Journal of *Marine Science and Engineering*

MDPI

Article

Simulation-Based Multiphysics Design and Adaptive Backstepping Control of a Dual-Propulsion Unmanned Aerial Underwater Vehicle

Ali Jebelli [1,*], Nafiseh Lotfi [2] and Mustapha C. E. Yagoub [3]

[1] School of Engineering and Technology, Kentucky State University, Frankfort, KY 40601, USA
[2] Department of Engineering and Design, Robotic Century Inc., Lexington, KY 40601, USA; nlotfi@roboticcentury.com
[3] School of Electrical Engineering and Computer Science, University of Ottawa, Ottawa, ON K1N 6N5, Canada; myagoub@uottawa.ca
* Correspondence: ali.jebelli@kysu.edu

Abstract

This study presents a simulation-based multiphysics design, modeling, and adaptive control framework for a dual-propulsion unmanned aerial underwater vehicle intended for aerial, near-surface, and fully submerged operation. The proposed platform uses four aerial rotors for flight and six underwater thrusters for submerged maneuvering, allowing medium-dependent actuation in air and water. Separate aerial and underwater six-degrees-of-freedom models are formulated and connected through a smooth altitude-dependent coordination strategy for the simplified near-surface region. Computational fluid dynamics is used to estimate submerged drag forces, while finite element analysis evaluates pressure-hull structural integrity at a depth of 20 m. At 0.2 m/s, the predicted horizontal and vertical drag forces are 1.62 N and 3.92 N, corresponding to quadratic damping coefficients of 40.5 and 98.0 $N \cdot s^2/m^2$. The FEA results show that PMMA provides a safety factor of 7.8, with a maximum displacement of 0.53 mm under hydrostatic loading. An adaptive backstepping controller with projected gain tuning, disturbance compensation, and constrained actuator allocation is developed. MATLAB/Simulink simulations demonstrate bounded trajectory tracking under nominal conditions, 20% parametric uncertainty, modeled disturbances, and a 0.5 m/s ocean current.

Keywords: unmanned aerial underwater vehicle; UAUV; hybrid aerial–underwater vehicle; dual-propulsion system; adaptive backstepping control; gradient-descent gain tuning; computational fluid dynamics; finite element analysis; hydrodynamic damping; trajectory tracking

Check for updates

Academic Editor: Huachao Dong

Received: 21 May 2026
Revised: 22 June 2026
Accepted: 25 June 2026
Published: 27 June 2026

Copyright: © 2026 by the authors. Licensee MDPI, Basel, Switzerland. This article is an open access article distributed under the terms and conditions of the Creative Commons Attribution (CC BY) license.

1. Introduction

Unmanned aerial underwater vehicles (UAUVs), also referred to as hybrid aerial–underwater vehicles (HAUVs), are robotic systems designed to operate across both aerial and aquatic environments. These vehicles combine the rapid deployment, wide-area mobility, and maneuverability of unmanned aerial vehicles (UAVs) with the underwater inspection, sensing, and navigation capabilities of autonomous underwater vehicles (AUVs) and remotely operated vehicles (ROVs) [1–4]. This cross-domain capability is valuable for environmental monitoring, coastal surveillance, offshore-structure inspection, search-and-rescue missions, marine data collection, and operations in locations where separate aerial

and underwater vehicles may be difficult to deploy efficiently [1–4]. Compared with using separate robotic platforms, a single UAUV can potentially reduce mission complexity by enabling an aerial approach, surface operation, submerged navigation, and return-to-air mission phases within one integrated system.

Despite these advantages, UAUV design and control remain difficult because air and water have substantially different physical properties. Water density is approximately three orders of magnitude greater than air density, which causes major changes in drag, buoyancy, added mass, actuator loading, propulsion efficiency, and vehicle response when the operating medium changes [1,3,5]. In aerial operation, vehicle performance is governed mainly by rotor-generated lift, attitude stability, aerodynamic drag, vehicle weight, and energy consumption. In underwater operation, the dominant effects instead include buoyancy, hydrodynamic damping, added mass, restoring forces, ocean-current disturbance, sealing reliability, and hydrostatic pressure resistance [5]. Therefore, a UAUV cannot be modeled simply as a waterproof quadrotor or as an underwater vehicle with added aerial rotors. Its mechanical configuration, dynamic model, propulsion system, and controller must be developed consistently for medium-dependent operation.

Several representative UAUV and HAUV platforms have been reported in the literature. Drews et al. presented an early modeling and simulation study of a quadrotor-like hybrid aerial–underwater vehicle [5]. Maia et al. introduced the Naviator concept and demonstrated a multirotor aerial–underwater vehicle capable of flight, underwater navigation, and transition maneuvers [6,7]. Alzu'bi et al. developed the Loon Copter, which uses active buoyancy control to support aerial, surface, and underwater operation [8]. Mercado et al. discussed aerial–underwater systems as a new paradigm in unmanned vehicles [9]. More recent studies have advanced HAUV development through gliding vehicles, real-ocean testing, tiltable propulsion units, and compact flexible aerial–aquatic platforms [10–13]. These works demonstrate significant progress in cross-medium vehicle design, but they also show that practical UAUV development still requires careful integration of propulsion layout, hydrodynamic modeling, pressure-hull assessment, transition coordination, and robust trajectory control.

From the control perspective, UAUVs require nonlinear and robust control strategies because their dynamics are strongly coupled, uncertain, and medium-dependent. Linear controllers may be effective near a limited operating point, but they are generally insufficient for multi-environment operation involving buoyancy variation, current disturbance, actuator reconfiguration, and model uncertainty. Nonlinear control methods, including backstepping, sliding-mode control, adaptive control, dynamic surface control, model predictive control, and fault-tolerant control, have been widely studied for aerial vehicles, underwater vehicles, and hybrid aerial–underwater systems [14,15]. Among these methods, backstepping is attractive because it provides a systematic Lyapunov-based design procedure for nonlinear systems. Adaptive extensions can further improve robustness by adjusting control parameters in response to uncertainty and disturbance effects. However, many existing studies focus on a specific vehicle prototype, a single operating medium, actuator-fault operation, or a transition-control problem. A unified simulation framework that connects medium-dependent modeling, hydrodynamic drag estimation, structural verification, actuator allocation, and adaptive trajectory tracking remains valuable for early-stage UAUV design.

The air–water transition is one of the most challenging parts of UAUV operation. During water entry and exit, the vehicle may experience free-surface deformation, splash disturbance, slamming load, propeller ventilation, partial submergence, rapidly changing buoyancy, and abrupt variation in actuator effectiveness [16–18]. These effects can cause instability if the model or controller switches abruptly between aerial and underwater

modes. Previous studies have investigated transition-aware planning, altitude control, and takeoff/landing strategies for hybrid aerial–underwater vehicles [16–18]. However, high-fidelity modeling of the complete transition process remains difficult because it involves coupled two-phase fluid dynamics, changing wetted area, actuator reconfiguration, and nonlinear vehicle motion. For this reason, the present study treats the transition region using a smooth altitude-dependent mission-level coordination model rather than a full two-phase CFD model. The transition results should, therefore, be interpreted as numerical behavior under the adopted control-oriented model, not as physical validation of real water-entry or water-exit hydrodynamics.

Underwater modeling also requires careful distinction between viscous drag and added mass. Drag is associated with motion at a given velocity and can be estimated using steady submerged CFD simulations. Added mass, in contrast, is acceleration-dependent and represents the inertia of the surrounding fluid that must be accelerated with the vehicle [19]. Therefore, the present study uses CFD specifically to estimate horizontal and vertical submerged drag forces and to obtain equivalent quadratic damping coefficients. The added-mass terms are included through the conventional marine-vehicle dynamic model under the ideal-fluid assumption, in which the fluid is treated as incompressible, inviscid, and irrotational [19]. Recent underwater-robot modeling work has also combined CFD-based hydrodynamic-coefficient estimation with strip-theory-based added-mass approximation, with subsequent coefficient tuning using genetic algorithms to reduce the simulation-to-experiment gap [20]. In the present study, uncertainty in the adopted added-mass and damping parameters is considered through the robustness simulations, while more detailed experimental tuning of the added-mass coefficients is identified as future work.

In addition to dynamic modeling, multiphysics analysis is important for reliable UAUV design. During underwater motion, hydrodynamic forces directly influence thruster sizing, damping coefficients, and trajectory-tracking performance. Computational fluid dynamics can be used to estimate drag forces, examine the flow field around submerged bodies, and support hydrodynamic design of AUVs [21–23]. Structural analysis is also required because the pressure hull must resist hydrostatic pressure at the intended operating depth. Previous underwater-vehicle studies have shown that hull material, sealing method, and depth resistance strategy strongly influence underwater vehicle reliability [24]. Finite element analysis, together with stress and displacement evaluation, provides a useful method for assessing hull deformation, material suitability, and safety factor under static pressure loading [25]. In many UAUV studies, CFD, FEA, and control design are treated as separate tasks. In contrast, the present work uses CFD-derived drag values in the underwater damping model and uses FEA results to support the material selection and rigid-hull assumption used in the control-oriented model.

Motivated by these challenges, this study presents a simulation-based multiphysics design and adaptive control framework for a dual-propulsion UAUV. The exact control objective is six-degrees-of-freedom trajectory tracking across aerial, near-surface/transition, and fully submerged mission phases under model uncertainty and external disturbances. The proposed vehicle uses four aerial rotors for flight and six underwater thrusters for submerged maneuvering. Separate aerial and underwater dynamic models are formulated to capture the dominant physical effects in each medium. A smooth altitude-dependent coordination function is introduced to connect the aerial and underwater model terms in the simplified near-surface region. CFD is used to estimate submerged drag forces, and FEA is used to evaluate pressure-hull integrity at a depth of 20 m. An adaptive backstepping controller with gradient-descent-based gain tuning is then developed to improve trajectory tracking under parametric uncertainty and modeled disturbances. The aerial part of the

model follows standard quadrotor rigid-body dynamics, while the underwater part follows a six-degrees-of-freedom marine-vehicle formulation with added mass, hydrodynamic damping, restoring forces, ocean-current-relative velocity, and thruster allocation [19,26,27].

The main contribution of this study is not the independent development of quadrotor dynamics, marine-vehicle modeling, CFD, FEA, or backstepping control, which are established techniques. The contribution is their integrated use in a single dual-propulsion UAUV framework with explicit information flow from physical design analysis to control-oriented simulation. The main contributions are summarized as follows:

1. A dual-propulsion UAUV configuration is developed using four aerial rotors and six underwater thrusters to support medium-dependent aerial and underwater operation.
2. Separate aerial and underwater six-degrees-of-freedom dynamic models are formulated and connected through a smooth altitude-dependent coordination strategy for mission-level near-surface simulation.
3. CFD-derived submerged drag forces are converted into numerical quadratic damping coefficients and inserted into the underwater dynamic model.
4. Strip-theory-based added-mass approximation is incorporated into the underwater dynamic model, while added-mass uncertainty is considered through parameter perturbation.
5. FEA-based pressure-hull assessment is performed at a depth of 20 m to support material selection and the rigid-body modeling assumption.
6. An adaptive backstepping trajectory-tracking controller with gradient-descent-based gain tuning, actuator constraints, and disturbance compensation is developed for the dual-propulsion UAUV model.
7. Numerical simulations evaluate nominal tracking, parametric uncertainty, modeled disturbances, ocean-current effects, transition-region response, and actuator feasibility constraints.

It should be emphasized that the present study is simulation-based. The transition model does not resolve full two-phase air–water flow, slamming, splash, propeller ventilation, or experimentally measured actuator degradation near the free surface. The CFD analysis is limited to submerged drag estimation, the added-mass model is based on a simplified strip-theory approximation, and the FEA analysis is limited to static hydrostatic loading. Prototype development, experimental validation, free-surface multiphase CFD, fluid–structure interaction, fatigue assessment, sealing evaluation, sensor-noise testing, actuator-delay analysis, genetic-algorithm tuning of hydrodynamic coefficients, and power-system characterization are identified as future work. These limitations are stated explicitly to avoid overclaiming the maturity of the proposed framework and to define clear directions for further development.

The remainder of this paper is organized as follows. Section 2 presents the UAUV body description and mathematical model. Section 3 describes the CFD and finite element analyses. Section 4 formulates the control problem. Section 5 develops the adaptive control strategy. Section 6 presents the simulation results and discussion. Section 7 concludes this study and outlines future work.

2. Body Description and Mathematical Model

2.1. System Description and Modeling Assumptions

The proposed unmanned aerial underwater vehicle is designed for aerial, near-surface or transition, and fully submerged operation. As illustrated in Figure 1, the vehicle adopts a dual-propulsion architecture composed of four aerial rotors and six underwater thrusters. The aerial rotors generate lift and attitude-control moments during flight, whereas the underwater thrusters provide the forces and moments required for submerged maneuvering.

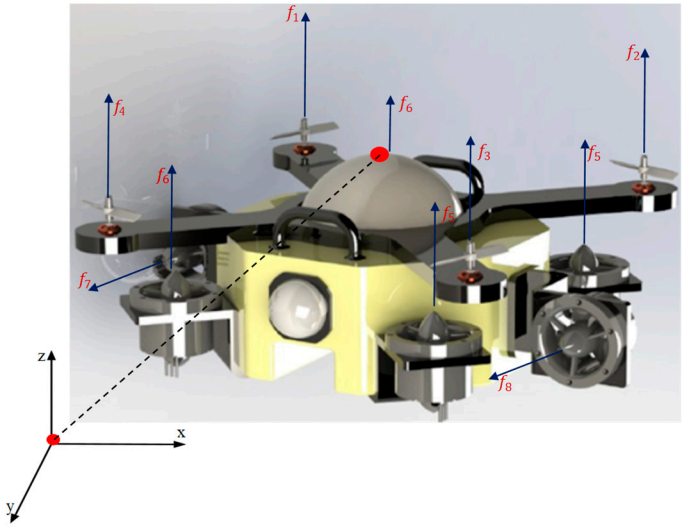


Figure 1. Three-dimensional model of the proposed unmanned aerial underwater vehicle, showing the four aerial rotors, six underwater thrusters, and body-fixed coordinate frame.

The vehicle structure consists of a compact central body containing the battery, electronics, sensors, and embedded control hardware inside a sealed pressure hull. The aerial and underwater propulsion systems are physically separated because air and water impose substantially different actuator loading, thrust generation efficiency, and hydrodynamic resistance. This dual-propulsion configuration avoids requiring one actuator type to operate efficiently in both media, but it introduces a coordination problem near the air–water interface.

The model assumes that the UAUV behaves as a rigid body with six degrees of freedom. The origin of the body-fixed frame is located at the vehicle center of mass, and the body axes are aligned with the principal inertia axes. Water is treated as incompressible over the considered operating-depth range. The aerial model is used when the vehicle is fully above the water surface, while the underwater model is used when the vehicle is fully submerged. Near the water surface, a smooth altitude-dependent transition function is used to avoid discontinuous switching between aerial and underwater model terms. Detailed two-phase air–water interface effects, including splash, slamming, surface tension, propeller ventilation, wave loading, and partial-submergence effects, are not explicitly resolved. These effects have been identified as important transition phenomena in previous HAUV studies [16–18].

The mean water surface is defined as $z = 0$, and the inertial z-axis is selected as positive upward. The aerial operating region is defined as z greater than or equal to +0.10 m. The near-surface transition region is defined as z between −0.10 m and +0.10 m. The fully submerged region is defined as z less than or equal to −0.10 m. Therefore, the transition half-width is 0.10 m. In the near-surface region, wind, wave effects, splash, propeller ventilation, partial submergence, and rapidly varying buoyancy may influence the vehicle. In the fully submerged region, buoyancy, added mass, hydrodynamic damping, and ocean currents are the dominant modeled effects.

The baseline numerical parameters used in the dynamic model and MATLAB/Simulink R2024b simulations are summarized in Table 1. The same parameter set is used in the nominal simulation, while selected mass, inertia, added-mass, damping, and actuator parameters are perturbed by ±20% in the robustness analysis.

The vehicle weight is 24.525 N, obtained from the 2.5 kg mass and gravitational acceleration of 9.81 m/s^2. The rotor thrust coefficient is consistent with a hover rotor speed of 700 rad/s. At the maximum rotor speed of 950 rad/s, the total available aerial thrust is

45.1 N, giving a thrust-to-weight ratio of 1.84. This provides sufficient thrust margin for aerial operation in the numerical model.

Table 1. Baseline numerical parameters used in the UAUV dynamic model.

Parameter	Symbol	Value	Unit
Vehicle mass	m	2.5	kg
Gravitational acceleration	g	9.81	m/s^2
Vehicle weight	W	24.525	N
Rotor arm length	l	0.20	m
Roll moment of inertia	Ix	3.50×10^{-2}	$kg \cdot m^2$
Pitch moment of inertia	Iy	3.65×10^{-2}	$kg \cdot m^2$
Yaw moment of inertia	Iz	6.00×10^{-2}	$kg \cdot m^2$
Rotor thrust coefficient	kf	1.25×10^{-5}	$N \cdot s^2/rad^2$
Rotor moment coefficient	km	2.00×10^{-7}	$N \cdot m \cdot s^2/rad^2$
Hover rotor speed	ωh	700	rad/s
Maximum rotor speed	ωmax	950	rad/s
Maximum total aerial thrust	Tmax	45.1	N
Thrust-to-weight ratio	Tmax/W	1.84	—
Added mass in surge	ma,u	0.38	kg
Added mass in sway	ma,v	0.55	kg
Added mass in heave	ma,w	0.95	kg
Added roll inertia	Ia,p	6.0×10^{-3}	$kg \cdot m^2$
Added pitch inertia	Ia,q	6.5×10^{-3}	$kg \cdot m^2$
Added yaw inertia	Ia,r	1.10×10^{-2}	$kg \cdot m^2$
Horizontal quadratic damping coefficient	dq,x	40.5	$N \cdot s^2/m^2$
Lateral quadratic damping coefficient	dq,y	40.5	$N \cdot s^2/m^2$
Vertical quadratic damping coefficient	dq,z	98.0	$N \cdot s^2/m^2$
Vertical-thruster longitudinal moment arm	at	0.12	m
Vertical-thruster lateral moment arm	bt	0.10	m
Horizontal-thruster yaw moment arm	bh	0.10	m
Underwater thruster coefficient	kt,i	20	N
Underwater thruster command range	ni	−1 to +1	—
Underwater thruster force limit	fwi,min, fwi,max	−20 to +20	N
Submerged volume	Vs	2.30×10^{-3}	m^3
Buoyancy force	B	22.56	N
Net underwater weight	W − B	1.96	N
Center of buoyancy relative to center of mass	xB, yB, zB	0, 0, 0.020	m
Transition half-width	ht	0.10	m
Water density	ρw	1000	kg/m^3
Parametric uncertainty level	δp	±20	%
Ocean-current magnitude	Vc	0.5	m/s

The submerged volume is 2.30×10^{-3} m^3. With a water density of 1000 kg/m^3 and gravitational acceleration of 9.81 m/s^2, this gives a buoyancy force of 22.56 N. The resulting net underwater weight is 1.96 N, which means that the vehicle is slightly negatively buoyant. This allows the UAUV to submerge while still requiring moderate upward thrust during ascent. The center of buoyancy is located 20 mm above the center of mass along the body-fixed z-axis to provide a passive restoring tendency in roll and pitch.

2.2. Reference Frames and Kinematics

Two coordinate frames are defined to describe the UAUV motion. This notation follows the standard marine-vehicle modeling convention [19]. The first is an inertial earth-fixed frame, denoted as FE = {X, Y, Z}. The second is a body-fixed frame, denoted as FB = {xb, yb, zb}, attached to the vehicle center of mass.

The generalized position and attitude vector contains the inertial position coordinates x, y, and z, and the roll, pitch, and yaw angles φ, θ, and ψ. The generalized body-fixed velocity vector contains the body-fixed linear velocities u, v, and w, and the body angular rates p, q, and r. The symbol ν is used for the complete body-fixed velocity vector to avoid confusion with the scalar lateral velocity v.

The kinematic relation maps the body-fixed velocity vector to the inertial position and attitude rates through a transformation matrix. This transformation contains the rotation matrix from the body-fixed frame to the inertial frame and the Euler-angle transformation matrix. A Z-Y-X Euler-angle convention is used. The Euler-angle transformation is valid for pitch angles smaller than ± 90 degrees. This formulation prevents the incorrect assumption that the body angular rates p, q, and r are identical to the Euler-angle derivatives.

2.3. Aerial Dynamics Model

In the aerial region, the UAUV behaves as a quadrotor-type vehicle. The aerial dynamics follow the standard multirotor rigid-body formulation [15,26,27]. The underwater thrusters are inactive in this region. The aerial control vector contains the total aerial thrust and the roll, pitch, and yaw control moments.

The aerial translational dynamics are written in the inertial frame. The vehicle acceleration is determined by gravity, the thrust vector generated by the aerial rotors, and lumped external aerial disturbances. The total rotor thrust acts along the body-fixed vertical axis and is rotated into the inertial frame using the vehicle attitude. The vertical acceleration includes gravitational acceleration and the vertical projection of the thrust. The vertical thrust projection is proportional to $\cos\theta \cos\varphi$, which is consistent with the upward-positive inertial z-axis.

The aerial rotational dynamics are written in the body-fixed frame. The angular acceleration depends on the rigid-body inertia matrix, gyroscopic coupling terms, commanded control moments, and lumped rotational disturbances. The rigid-body inertia matrix is diagonal, with roll inertia equal to 3.50×10^{-2} kg·m^2, pitch inertia equal to 3.65×10^{-2} kg·m^2, and yaw inertia equal to 6.00×10^{-2} kg·m^2.

The aerial rotor allocation maps the squared rotor speeds to total thrust and body moments. The rotor thrust coefficient is 1.25×10^{-5} N·s^2/rad^2, the rotor moment coefficient is 2.00×10^{-7} N·m·s^2/rad^2, and the rotor-arm length is 0.20 m. The physical rotor speeds are constrained to remain between 0 and 950 rad/s. Therefore, signed pre-allocation variables are not interpreted as physical rotor speeds. The physical rotor speeds used in the actuator model are always non-negative.

2.4. Fully Submerged Dynamic Model

In the fully submerged region, the UAUV is represented using a nonlinear six-degrees-of-freedom marine-vehicle model. This formulation follows the standard six-degrees-of-freedom marine craft model [19]. The underwater dynamic model includes rigid-body inertia, added mass, Coriolis and centripetal effects, hydrodynamic damping, restoring forces and moments, underwater control input, and underwater disturbance input.

The generalized position and attitude vector contains the inertial position coordinates x, y, and z and the roll, pitch, and yaw angles. The body-fixed velocity vector contains the linear velocity components u, v, and w and the angular velocity components p, q, and r. In compact form, the fully submerged equation of motion states that the total underwater inertia multiplied by the body acceleration, plus the Coriolis and centripetal terms, hydrodynamic damping terms, and restoring-force terms, is equal to the generalized underwater control wrench plus the underwater disturbance wrench. The hydrodynamic

damping terms are evaluated using the current-relative velocity so that ocean-current effects are included in the underwater model.

The total underwater inertia is composed of the rigid-body inertia and the added-mass contribution. The rigid-body inertia uses the vehicle mass of 2.5 kg and the roll, pitch, and yaw moments of inertia listed in Table 1. The added-mass contribution is included because the surrounding water must be accelerated together with the vehicle during submerged motion.

For the added-mass approximation, the submerged UAUV body is treated as a compact, approximately symmetric, rounded pressure-hull body with external arms and thruster supports. In the control-oriented model, the main submerged volume is approximated by an equivalent prolate cylindrical or ellipsoidal body divided into longitudinal strips. The sectional added-mass contributions are estimated using strip-theory reasoning and assembled into diagonal surge, sway, heave, roll, pitch, and yaw added-inertia terms. The external arms and thruster supports are retained in the CFD drag estimation, while their uncertainty in the added-mass model is represented through the $\pm 20\%$ parameter perturbation used in the robustness analysis. This approach is consistent with recent underwater-robot modeling practice in which CFD is used for hydrodynamic drag estimation and strip theory is used for added-mass approximation [20]. In future experimental trials, the added-mass coefficients can be further tuned using optimization methods such as a genetic algorithm to reduce the difference between simulation and prototype response.

The added-mass values used in the baseline model are 0.38 kg in surge, 0.55 kg in sway, and 0.95 kg in heave. The added rotational inertias are 6.0×10^{-3} kg·m^2 in roll, 6.5×10^{-3} kg·m^2 in pitch, and 1.10×10^{-2} kg·m^2 in yaw. Therefore, the resulting total underwater inertia values are 2.88 kg in surge, 3.05 kg in sway, and 3.45 kg in heave. The corresponding total roll, pitch, and yaw inertias are 4.10×10^{-2} kg·m^2, 4.30×10^{-2} kg·m^2, and 7.10×10^{-2} kg·m^2, respectively.

The added-mass submodel follows the classical marine-vehicle ideal-fluid approximation, in which the surrounding fluid is assumed to be incompressible, inviscid, and irrotational [19,20]. The added mass is not obtained from the steady CFD drag simulations. The CFD results are used only to estimate geometry-dependent viscous drag and to define the hydrodynamic damping coefficients. Uncertainty in the adopted added-mass terms is included in the robustness analysis.

The underwater hydrodynamic damping model includes linear and quadratic damping terms. The dominant translational quadratic damping coefficients are obtained from the CFD analysis. The horizontal damping coefficient is 40.5 N·s^2/m^2, the lateral damping coefficient is taken as 40.5 N·s^2/m^2, and the vertical damping coefficient is 98.0 N·s^2/m^2. Therefore, the vertical damping is approximately 2.42-times larger than the horizontal damping. This is consistent with the larger vertical projected area observed in the CFD analysis. The lateral damping coefficient is initially taken equal to the horizontal value because a dedicated lateral-flow CFD case was not conducted. The rotational damping terms are treated as bounded uncertain model parameters in the robustness analysis because dedicated rotational CFD cases were also not conducted.

The underwater generalized control input is generated by six underwater thrusters. The first four underwater thrusters are modeled as vertical thrusters for heave, roll, and pitch control. The last two thrusters are modeled as horizontal thrusters for surge and yaw control. The vertical-thruster longitudinal moment arm is 0.12 m, the vertical-thruster lateral moment arm is 0.10 m, and the horizontal-thruster yaw moment arm is 0.10 m.

The present thruster layout provides direct actuation in surge, heave, roll, pitch, and yaw. Lateral motion is not independently actuated and is regulated indirectly through yaw, surge motion, hydrodynamic damping, and trajectory control.

Each underwater thruster is modeled using a normalized reversible command ranging from negative one to positive one. The corresponding thruster force range is from negative 20 N to positive 20 N. This force limit is used in the actuator feasibility analysis and constrained allocation.

The buoyancy force is 22.56 N, based on the submerged volume of 2.30×10^{-3} m^3. The vehicle weight is 24.525 N, giving a net underwater weight of 1.96 N. The center of buoyancy is located at 0, 0, and 0.020 m relative to the center of mass. This vertical offset provides a passive restoring tendency in roll and pitch during submerged operation.

2.5. Ocean-Current Disturbance Model

Ocean currents are included using a relative-velocity formulation. This is consistent with standard marine-vehicle modeling practice, in which hydrodynamic damping is evaluated using the velocity relative to the surrounding fluid [19]. The relative velocity is defined as the vehicle body-fixed velocity minus the current velocity expressed in the body-fixed frame. If the current is originally defined in the inertial frame, it is transformed into the body-fixed frame using the transpose of the rotation matrix.

The current direction is represented using a current magnitude, a horizontal direction angle, and a vertical direction angle. In the principal disturbed simulation, the current magnitude is 0.5 m/s, the horizontal direction angle is zero, and the vertical direction angle is zero. This corresponds to a current aligned with the inertial X-direction. The hydrodynamic damping terms are evaluated using the relative velocity, while the vehicle acceleration remains defined by the vehicle body-fixed acceleration.

2.6. Near-Surface and Transition Modeling

A discontinuous switch at the water surface can produce unrealistic numerical behavior because the real vehicle experiences partial submergence, changing buoyancy, changing drag, splash, and changing actuator effectiveness near the interface. To reduce this discontinuity at the model level, a smooth submergence function is introduced.

The submergence ratio is zero when the vehicle is fully aerial, one when the vehicle is fully submerged, and smoothly varies between zero and one inside the near-surface transition region. The transition half-width is 0.10 m, meaning that the transition region extends from 0.10 m above the mean water surface to 0.10 m below it.

The aerial weighting factor is defined as one minus the submergence ratio, while the underwater weighting factor is equal to the submergence ratio. These two weighting factors always remain between zero and one and always sum to one. Therefore, the aerial contribution gradually decreases as the vehicle enters the water, while the underwater contribution gradually increases.

The aerial generalized wrench includes vertical thrust and roll, pitch, and yaw moments. In the near-surface region, the effective actuator wrench is approximated by blending the aerial wrench and the underwater wrench using the altitude-dependent weighting factors. The mass, damping, and buoyancy terms are also introduced gradually according to the same submergence weighting.

The simplified near-surface model includes an additional bounded transition disturbance term. This term represents unresolved effects, such as wave and wind loading, splash, slamming, propeller ventilation, partial submergence, rapid changes in wetted area, and variation in actuator effectiveness. The weighting functions are used only for mission-level control coordination. Similar smooth transition concepts have been used in prior hybrid aerial–underwater vehicle studies to reduce abrupt switching near the air–water interface [16–18]. They are not intended to represent experimentally identified propulsor efficiency curves or a high-fidelity two-phase free-surface model. Therefore, the

transition simulation results should be interpreted as bounded response under the adopted control-oriented model, not as physical validation of water-entry or water-exit hydrodynamics.

2.7. Governing Equations of Motion

To preserve the mathematical rigor of the dynamic model, the principal equations of motion are summarized in this subsection in compact form. The generalized position and attitude vector contains the inertial position coordinates x, y, and z and the Euler angles roll, pitch, and yaw. The body-fixed velocity vector contains the linear velocity components u, v, and w and the angular velocity components p, q, and r. The kinematic relation maps the body-fixed velocity vector to the inertial position and attitude rates through the transformation matrix J(η), which contains the body-to-inertial rotation matrix and the Euler-angle transformation matrix.

For aerial operation, the translational dynamics are governed by the balance among vehicle weight, rotor-generated thrust, and lumped external disturbance force. The aerial translational equation can be written in compact form as vehicle mass multiplied by inertial acceleration equals the gravitational force, plus the aerial thrust vector rotated into the inertial frame, plus the lumped aerial disturbance force. In this model, the total aerial thrust acts along the body-fixed vertical axis and is projected into the inertial frame using the attitude rotation matrix.

The aerial rotational dynamics are written in the body-fixed frame. The angular acceleration is governed by the rigid-body inertia matrix, gyroscopic coupling terms, commanded roll, pitch, and yaw moments, and lumped rotational disturbance moments. For the diagonal inertia matrix used in this study, the roll, pitch, and yaw angular accelerations depend on the corresponding control moments, the inertial coupling among p, q, and r, and the bounded rotational disturbances.

The aerial rotor allocation maps the squared rotor speeds to the total aerial thrust and the three body moments. The physical rotor speeds are constrained to remain between 0 and 950 rad/s. Therefore, signed intermediate control or allocation variables are not interpreted as physical rotor speeds. Only the final constrained non-negative rotor speeds are used as physical actuator commands.

For fully submerged operation, the UAUV follows a six-degrees-of-freedom marine-vehicle dynamic model. In compact form, the underwater equation of motion states that the total underwater inertia multiplied by the body-fixed acceleration, plus the Coriolis and centripetal terms, hydrodynamic damping terms, and restoring-force terms, is equal to the generalized underwater control wrench plus the lumped underwater disturbance wrench. The hydrodynamic damping terms are evaluated using the current-relative velocity, which is defined as the body-fixed vehicle velocity minus the current velocity expressed in the body-fixed frame.

The total underwater inertia matrix is the sum of the rigid-body inertia matrix and the added-mass matrix. The added-mass matrix used in the baseline model contains the added-mass values in surge, sway, and heave and the added rotational inertias in roll, pitch, and yaw. These values are included in Table 1. The added-mass model represents the acceleration-dependent fluid inertia associated with submerged motion, while the CFD-derived drag coefficients represent velocity-dependent hydrodynamic resistance.

The underwater damping model includes linear and quadratic damping terms. The dominant translational quadratic damping coefficients are obtained from the CFD analysis. The horizontal and lateral damping coefficients are 40.5 $N \cdot s^2/m^2$, while the vertical damping coefficient is 98.0 $N \cdot s^2/m^2$. Therefore, the model accounts for the higher hydrodynamic resistance during vertical motion compared with horizontal motion.

The underwater control wrench is generated by the six underwater-thruster forces through the underwater allocation matrix. The first four thrusters provide heave, roll, and pitch control, while the last two thrusters provide surge and yaw control. Each underwater thruster is constrained to generate force from negative 20 N to positive 20 N. These force limits are used in the constrained actuator allocation and actuator feasibility analysis.

In the near-surface region, the model uses a smooth altitude-dependent blending approach. The effective actuator wrench is formed by combining the aerial wrench and underwater wrench using the aerial and underwater weighting factors. The medium-dependent inertia, damping, buoyancy, and actuation terms are also introduced gradually according to the same transition weighting functions. This avoids abrupt switching at the water surface and provides a continuous mission-level model for simulation and control design.

The near-surface equation of motion can, therefore, be interpreted as a blended dynamic model in which the altitude-dependent inertia, damping, restoring-force, and actuator terms act together with bounded transition disturbance terms. These transition disturbance terms represent unresolved effects, such as splash, slamming, partial submergence, propeller ventilation, wave loading, and rapid variation in actuator effectiveness. The model is used only for control-oriented mission simulation and is not intended to represent high-fidelity two-phase free-surface hydrodynamics.

Finally, the uncertainty model perturbs selected baseline parameters by $\pm 20\%$. The perturbed parameters include mass, rigid-body inertia, added mass, hydrodynamic damping, and selected actuator coefficients. This uncertainty model is used in the disturbed simulation cases to evaluate robustness of the proposed controller to modeling errors and environmental disturbances.

Overall, this subsection summarizes the main aerial rigid-body dynamics, fully submerged marine-vehicle dynamics, actuator allocation relationships, simplified near-surface blended dynamics, and parameter-uncertainty model used for simulation and control design.

2.8. Control-Oriented State–Space Representation

For aerial operation, the state vector contains the vehicle position, translational velocity, attitude, and angular velocity. The aerial dynamics can be written in a nonlinear state–space form that includes the nominal aerial dynamics, the aerial input distribution matrix, the aerial control vector, and lumped disturbances.

For fully submerged operation, the state vector contains the generalized position and attitude vector and the body-fixed velocity vector. The underwater dynamics can also be written in nonlinear state–space form using the underwater model, the current-relative velocity, the underwater control input, and lumped underwater disturbances.

For near-surface operation, the state–space model includes both aerial and underwater control contributions. The aerial and underwater input effects are weighted by the altitude-dependent transition functions. This representation provides the mapping between the physical vehicle model and the nonlinear control formulation developed in Sections 4 and 5.

2.9. Multiphysics Coupling with CFD and FEA

The mathematical model is connected to the multiphysics analyses through the hydrodynamic damping and structural validity assumptions. The CFD simulations in Section 3 provide the submerged drag forces at a representative velocity of 0.2 m/s. CFD-based drag estimation is widely used to support hydrodynamic modeling and design of underwater vehicles [21–23]. The computed horizontal and vertical drag forces are 1.62 N and 3.92 N, respectively.

Using the quadratic drag relation, these drag forces correspond to damping coefficients of 40.5 $N \cdot s^2/m^2$ in the horizontal direction and 98.0 $N \cdot s^2/m^2$ in the vertical direction. These values are inserted into the underwater damping model.

The FEA analysis evaluates the pressure-hull response at a depth of 20 m. Von Mises stress and displacement evaluation are standard tools for preliminary structural assessment under static loading [25]. At this depth, the hydrostatic gauge pressure is 196.2 kPa. The FEA results are used to support the rigid-body hull assumption and material selection, while the CFD results are used to support the hydrodynamic damping model. The CFD and FEA analyses do not replace prototype validation.

2.10. Parameter Uncertainty Model

To evaluate robustness to modeling uncertainty, selected parameters are perturbed by $\pm 20\%$ relative to their baseline values. The perturbed parameters include vehicle mass, rigid-body inertia, added mass, hydrodynamic damping, and selected actuator coefficients. This uncertainty model is used in the disturbed simulation cases to examine the sensitivity of the controller to modeling errors.

2.11. Model Limitations

The model does not include high-fidelity two-phase air–water flow, wave–body interaction, slamming-impact modeling, propeller ventilation modeling, experimentally identified actuator efficiency loss near the free surface, depth-varying current profiles, fluid–structure interaction, structural flexibility, sensor dynamics, actuator delay, or power-system dynamics. These effects are identified as future work and are not claimed as validated in the present simulation-based study.

In addition, the CFD analysis identifies dominant horizontal and vertical translational drag terms. Dedicated lateral-flow, rotational-flow, forced-oscillation, or experimental tests would be required to identify the complete six-degrees-of-freedom hydrodynamic model with higher fidelity.

2.12. Summary of the Mathematical Model

This section formulated the dual-propulsion UAUV as a medium-dependent six-degrees-of-freedom system. The aerial model uses quadrotor rigid-body dynamics with the correct vertical thrust projection and explicit separation between Euler-angle rates and body angular rates. The underwater model separates rigid-body inertia, ideal-fluid added mass, CFD-informed damping, restoring forces, current-relative velocity, and underwater-thruster allocation. A near-surface region was introduced to distinguish partial-submergence operation from fully submerged motion, and a smooth altitude-dependent function was used to coordinate the aerial and underwater dynamics without claiming high-fidelity free-surface resolution. The resulting state–space representation is used for the control problem formulation and adaptive controller design in Sections 4 and 5.

3. CFD and Finite Element Analysis

The multiphysics analysis was performed to support the underwater dynamic model and to evaluate the structural suitability of the proposed UAUV pressure hull. Computational fluid dynamics was used to estimate submerged hydrodynamic drag forces, while finite element analysis was used to evaluate hull stress and deformation under hydrostatic pressure at the target operating depth.

The analyses in this section focus on the fully submerged condition. The air–water transition region is not modeled as a two-phase free-surface CFD problem in the present study. Effects, such as splash, slamming, wave interaction, propeller ventilation, rapidly changing wetted area, and partial submergence, are, therefore, not directly resolved. In-

stead, these effects are treated as bounded disturbances in the transition model and are discussed as limitations of the present simulation-based study.

The CFD results are used only for viscous and pressure-drag estimation. They are not used to identify added mass. Added mass is acceleration-dependent and is represented in Section 2 using a conventional marine-vehicle ideal-fluid model. This distinction is important because steady submerged CFD simulations at constant velocity do not directly provide acceleration-dependent added-mass coefficients.

3.1. Hydrodynamic CFD Model

During fully submerged motion, the UAUV experiences hydrodynamic forces that influence thruster sizing, damping-model identification, and trajectory-tracking performance. Therefore, CFD simulations were conducted for representative horizontal and vertical submerged motions. The flow was modeled as three-dimensional, steady, incompressible, single-phase turbulent flow around the UAUV body.

The governing flow model was based on the steady Reynolds-averaged Navier–Stokes formulation for incompressible flow. The shear-stress-transport k–ω turbulence model was used because it provides reliable near-wall behavior and improved prediction capability for separated flow and adverse pressure-gradient regions [21]. The fluid was modeled as water with a density of 1000 kg/m^3 and a dynamic viscosity of 1.0×10^{-3} Pa·s.

The representative submerged velocity used in the CFD simulations was 0.2 m/s. The characteristic length was taken as 0.20 m, corresponding to the representative body scale used in the dynamic model. Based on these values, the Reynolds number is 4.0×10^4. This indicates that the simulated submerged cases correspond to a turbulent-flow regime around the representative UAUV body scale.

The CAD model was prepared by retaining the main hydrodynamic surfaces of the UAUV, including the pressure hull, external arms, and underwater-thruster supports. Small geometric details that do not significantly influence the global flow field were simplified to improve mesh quality and numerical stability. The computational domain was extended several characteristic lengths away from the vehicle to reduce blockage effects.

A uniform velocity inlet was applied at the upstream boundary, and a static pressure outlet was applied at the downstream boundary. The far-field boundaries were placed sufficiently far from the vehicle to reduce artificial confinement effects. A no-slip wall boundary condition was applied to the UAUV surface. The pressure–velocity coupling was solved using a coupled scheme, and second-order upwind discretization was used for the momentum and turbulence equations.

The CFD setup is summarized in Table 2.

The computational domain and mesh distribution are shown in Figure 2. Local mesh refinement was applied near the pressure hull, rotor arms, underwater-thruster supports, and regions of expected pressure-gradient concentration. Boundary-layer refinement was used near the wetted vehicle surface to improve the near-wall flow resolution.

Because the CFD simulations were formulated as steady-state RANS cases, a physical transient time-step independence study was not applicable to the CFD calculations. The time-step sensitivity relevant to the controller simulation is associated with the MATLAB/Simulink numerical integration and is addressed separately in the simulation results section.

The selected mesh contained approximately one million tetrahedral elements with local refinement near the UAUV body. The residual convergence criterion was set to 1.0×10^{-4}, and the integrated drag force was monitored as the main engineering output. The selected mesh resolution, near-wall refinement, convergence criterion, and drag-force monitoring are reported explicitly to improve reproducibility. A complete grid convergence study

using multiple independently generated meshes would further improve hydrodynamic verification. In the present study, the CFD results should, therefore, be interpreted as design-level drag estimates for the control-oriented model rather than final mesh-independent hydrodynamic certification. The absence of dedicated lateral-flow, rotational-flow, and forced-oscillation CFD cases is identified as a limitation.

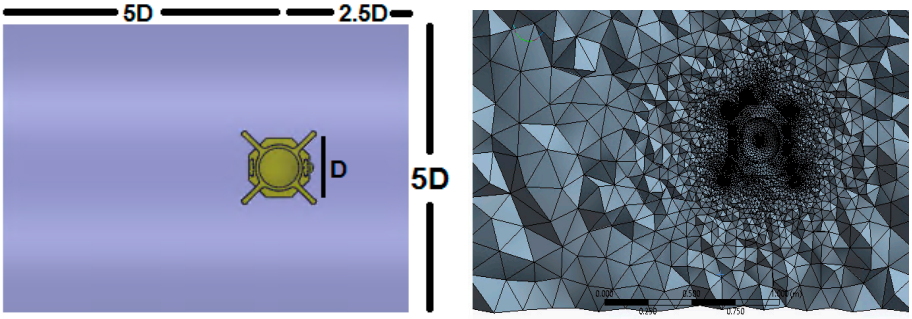


Figure 2. Computational domain and mesh distribution used in the submerged CFD analysis of the UAUV.

Table 2. CFD setup and boundary conditions.

Parameter	Description/Value
Flow domain	Fully submerged single-phase water domain
Flow dimensionality	Three-dimensional
Flow model	Steady incompressible RANS
Turbulence model	SST k–ω
Fluid	Water
Water density	1000 kg/m^3
Dynamic viscosity	1.0×10^{-3} Pa·s
Representative velocity	0.2 m/s
Characteristic length	0.20 m
Reynolds number	4.0×10^4
Simulated cases	Horizontal and vertical submerged motion
Inlet boundary condition	Uniform velocity inlet
Outlet boundary condition	Static pressure outlet
Vehicle surface condition	No-slip wall
Far-field boundaries	Placed several body lengths from the UAUV to reduce blockage
Mesh type	Tetrahedral volume mesh with local refinement
Approximate element count	Approximately 1.0×10^6 elements
Near-wall treatment	Local boundary-layer refinement near the UAUV body
Pressure–velocity coupling	Coupled scheme
Spatial discretization	Second-order upwind for momentum and turbulence equations
Residual convergence criterion	1.0×10^{-4}
Monitored output	Integrated pressure and viscous drag force

3.2. CFD Drag-Force Results

CFD simulations were conducted for horizontal and vertical submerged motion at a representative velocity of 0.2 m/s. The horizontal case represents forward submerged navigation, while the vertical case represents ascent, descent, and depth control motion. The velocity contours are shown in Figure 3.

The drag force was calculated by integrating the pressure and viscous stresses over the wetted surface of the vehicle in the direction of motion. CFD-based drag estimation is commonly used to support hydrodynamic modeling and design of underwater vehicles [20,22]. The computed drag forces are summarized in Table 3.

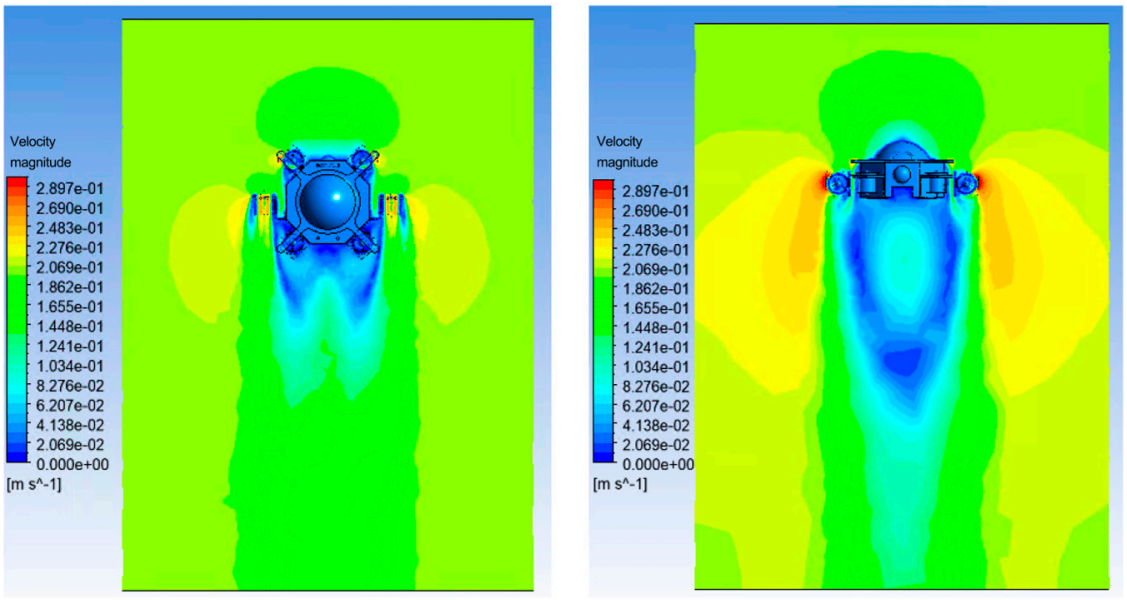


Figure 3. Velocity contours around the UAUV during: (**a**) horizontal submerged motion and (**b**) vertical submerged motion. The color bar represents velocity magnitude in m s^{-1}.

Table 3. Hydrodynamic drag forces obtained from CFD at 0.2 m/s.

Motion Type	Representative Velocity	Dominant Drag Force	Equivalent Quadratic Damping Coefficient	Observation
Horizontal motion	0.2 m/s	1.62 N	40.5 N·s^2/m^2	Dominant in longitudinal direction; lower projected area
Vertical motion	0.2 m/s	3.92 N	98.0 N·s^2/m^2	Dominant in vertical direction; higher projected area

The results show that vertical motion produces a larger drag force than horizontal motion. At 0.2 m/s, the vertical drag force is 3.92 N, while the horizontal drag force is 1.62 N. Therefore, the vertical drag is approximately 2.42-times larger than the horizontal drag. This difference is mainly caused by the larger projected area exposed to the flow during vertical motion.

To connect the CFD results directly to the underwater dynamic model, the drag forces were converted into equivalent quadratic damping coefficients. The horizontal drag force of 1.62 N at 0.2 m/s gives a horizontal quadratic damping coefficient of 40.5 N·s^2/m^2. The vertical drag force of 3.92 N at 0.2 m/s gives a vertical quadratic damping coefficient of 98.0 N·s^2/m^2. These coefficients are inserted into the underwater damping model introduced in Section 2.

Since dedicated lateral-flow and rotational CFD cases were not conducted, the lateral damping coefficient is initially taken equal to the horizontal damping coefficient, while rotational damping terms are treated as uncertain model parameters in the robustness analysis. This approach improves the physical consistency of the underwater dynamic model while clearly identifying the hydrodynamic terms that still require future identification.

3.3. Structural FEA Model

Finite element analysis was performed to evaluate the structural integrity of the UAUV pressure hull under hydrostatic loading. The target operating depth was selected as 20 m.

At this depth, the hydrostatic gauge pressure is 196.2 kPa, based on a water density of 1000 kg/m^3 and gravitational acceleration of 9.81 m/s^2.

The external hydrostatic pressure was applied uniformly to the wetted surface of the pressure hull. The internal pressure was assumed to remain atmospheric; therefore, the applied pressure represents the external gauge-pressure load. The analysis was performed as a static, linear-elastic structural analysis. The purpose was to compare candidate hull materials under hydrostatic loading and to verify whether the resulting deformation is small enough to support the rigid-body assumption used in the control-oriented dynamic model.

The structural response was evaluated using maximum von Mises stress, maximum displacement, and safety factor. The safety factor was calculated by comparing the material yield strength with the maximum von Mises stress obtained from the FEA solution. Von Mises stress and displacement evaluation are standard tools for preliminary structural assessment under static loading [24].

The FEA setup is summarized in Table 4.

Table 4. FEA setup and boundary conditions.

Parameter	Description/Value
Analysis type	Static linear-elastic structural analysis
Target depth	20 m
Applied external pressure	196.2 kPa
Load direction	Normal to external wetted pressure-hull surfaces
Internal pressure	Atmospheric reference pressure
Failure criterion	Maximum von Mises stress
Safety factor	Material yield strength divided by maximum von Mises stress
Candidate materials	HDPE, PMMA, PTFE, and POM-C with 10% glass reinforcement
Element type	Solid tetrahedral elements
Mesh refinement	Refined near openings, mounting regions, geometric discontinuities, and stress-concentration regions
Constraint treatment	Minimal displacement constraints applied at mounting/support interfaces to remove rigid-body motion
Effects not included	Impact, fatigue, buckling, sealing failure, manufacturing defects, FSI, and slamming load

The boundary-condition strategy was selected to avoid unrealistic free-body motion while limiting artificial stiffening of the pressure hull. Constraints were applied only at support or mounting regions that represent physical attachment locations in the vehicle assembly. Mesh refinement was applied near openings, mounting features, geometric discontinuities, and regions where stress concentration was expected.

The FEA analysis does not represent full structural certification. It evaluates the pressure-hull response under static hydrostatic loading at the selected depth only. Additional testing would be required to assess impact resistance, cyclic fatigue, sealing reliability, manufacturing defects, buckling, and fluid–structure interaction.

3.4. Material Selection and FEA Results

Four candidate polymer materials were evaluated for the pressure hull: HDPE, PMMA, PTFE, and POM-C with 10% glass reinforcement. The von Mises stress distributions are shown in Figure 4.

The quantitative FEA results are summarized in Table 5. The material-property values were selected from standard engineering material data used for preliminary structural comparison [28].

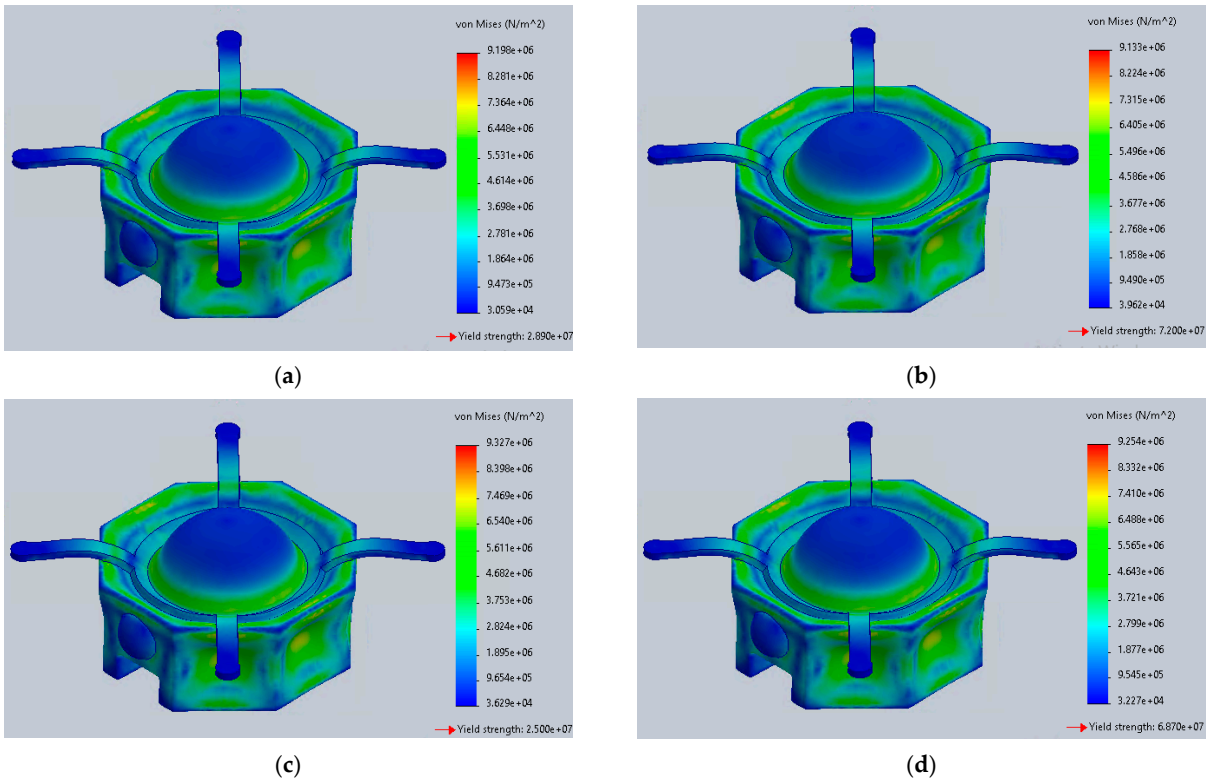


Figure 4. Von Mises stress distribution of the UAUV hull for different materials: (**a**) HDPE, (**b**) PMMA, (**c**) PTFE, and (**d**) POM-C with 10% glass reinforcement.

Table 5. Material properties and FEA results under hydrostatic pressure at 20 m depth.

Material	Density	Water Absorption	Empty Hull Weight	Yield Strength	Maximum Von Mises Stress	Safety Factor	Maximum Displacement
HDPE	954 kg/m^3	0.015%	4.32 kg	28.9 MPa	9.32 MPa	3.1	1.67 mm
PMMA	1190 kg/m^3	0.4%	5.39 kg	72.0 MPa	9.23 MPa	7.8	0.53 mm
PTFE	2290 kg/m^3	0.065%	10.4 kg	20.5 MPa	7.88 MPa	2.6	2.40 mm
POM-C, 10% glass reinforced	1410 kg/m^3	0.2%	6.38 kg	68.7 MPa	9.28 MPa	7.4	0.31 mm

To further illustrate the structural response of the selected material, the displacement distribution of the PMMA hull is shown in Figure 5.

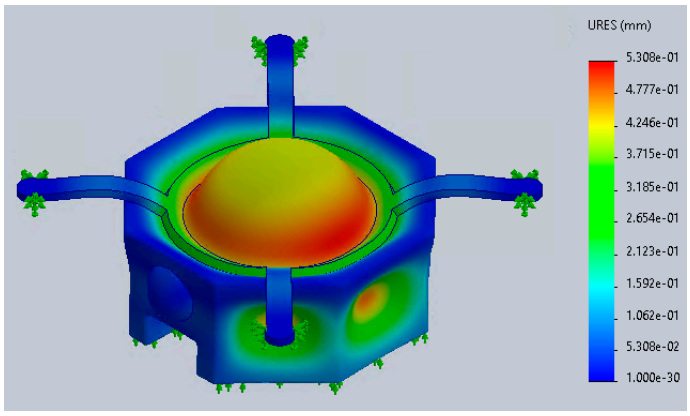


Figure 5. Displacement contour of the UAUV hull made of PMMA under hydrostatic pressure at 20 m depth.

All evaluated materials satisfy the basic static structural requirement for the target depth of 20 m under the adopted assumptions, but they differ significantly in safety margin, deformation, density, water absorption, and practical suitability. PTFE has the lowest safety factor and the largest displacement, making it less suitable for the present pressure-hull application. HDPE has the lowest density but produces higher deformation than PMMA and POM-C. POM-C with 10% glass reinforcement provides the lowest maximum displacement, 0.31 mm, but its safety factor is slightly lower than that of PMMA and its density is higher than that of HDPE and PMMA.

PMMA was selected as the preferred hull material because it provides the highest safety factor, 7.8, with a moderate maximum displacement of 0.53 mm. PMMA also offers practical advantages during prototype testing because its transparency can support visual inspection of leakage, condensation, and internal component arrangement. However, PMMA is more brittle than some polymer alternatives; therefore, impact resistance, sealing reliability, and fatigue performance should be experimentally verified in future prototype tests.

3.5. Coupling of CFD and FEA Results with the Dynamic Model

The CFD and FEA analyses were integrated into the modeling workflow rather than treated as independent design checks. The CFD drag forces were converted into equivalent quadratic damping coefficients and inserted into the underwater damping matrix introduced in Section 2. Therefore, the underwater model accounts for the fact that vertical submerged motion experiences stronger hydrodynamic resistance than horizontal motion.

The FEA results support the rigid-body assumption used in the underwater dynamic model. For the selected PMMA hull, the maximum displacement under hydrostatic pressure at 20 m depth is 0.53 mm, which is small relative to the overall hull dimensions. Therefore, hull deformation is neglected in the nominal underwater dynamic model, and buoyancy is calculated using the undeformed submerged volume.

For deeper operation or more flexible hull designs, deformation-induced volume change should be considered. In that case, the buoyancy and restoring-force terms would need to be updated using the depth-dependent volume change obtained from structural deformation analysis. This extension would allow the FEA deformation result to update the buoyancy model directly.

3.6. Discussion and Limitations

The CFD results show that vertical underwater motion produces a higher drag force than horizontal motion. This finding is important for thruster sizing and controller design because ascent and descent maneuvers require stronger compensation against hydrodynamic resistance. The conversion of drag forces into quadratic damping coefficients improves the physical consistency of the underwater dynamic model.

The CFD analysis is limited to fully submerged single-phase steady flow. It does not model the air–water interface, free-surface deformation, wave interaction, splash, surface tension, slamming load, propeller ventilation, or changing propulsor efficiency during water entry and exit. The propeller-induced flow field is also not explicitly resolved. In addition, only horizontal and vertical translational drag cases were evaluated. Dedicated lateral-flow, rotational-flow, forced-oscillation, or experimental tests would be required to identify the complete six-degrees-of-freedom hydrodynamic model, including rotational damping and acceleration-dependent added mass.

The FEA results show that the pressure hull can withstand the static hydrostatic pressure corresponding to the target depth of 20 m under the adopted linear-elastic assumptions. Among the evaluated materials, PMMA provides the highest safety factor with moderate

deformation and practical prototype advantages. However, the FEA analysis is limited to static pressure loading. It does not include impact loading, cyclic fatigue, buckling, sealing failure, manufacturing defects, fluid–structure interaction, long-term water exposure, or water-entry slamming loads.

Future work should, therefore, include free-surface multiphase CFD, lateral and rotational hydrodynamic identification, forced-oscillation or experimental added-mass estimation, propeller-flow modeling, mesh convergence refinement, fluid–structure interaction, pressure-chamber testing, sealing assessment, fatigue analysis, and experimental validation of the prototype hull.

4. Problem Formulation and Control Objectives

The objective of the control system is to achieve six-degrees-of-freedom trajectory tracking for the proposed UAUV across aerial, near-surface or transition, and fully submerged operating regions. The controller must maintain bounded tracking performance under parametric uncertainty, hydrodynamic damping uncertainty, ocean-current disturbance, modeled external disturbances, actuator constraints, and the simplified altitude-dependent transition model introduced in Section 2.

Unlike a conventional UAV or AUV control problem, the present UAUV requires coordination between two physically different propulsion systems. The aerial rotors dominate the control authority during flight, while the underwater thrusters dominate the control authority during submerged operation. In the near-surface region, both the model terms and actuator contributions vary gradually according to the transition weighting function. Therefore, the control problem is formulated as a mode-dependent nonlinear trajectory-tracking problem with actuator constraints and bounded disturbances.

4.1. Mode-Dependent Nonlinear System Form

The UAUV operates in three regions: aerial operation, near-surface or transition operation, and fully submerged operation. These regions are defined according to the vehicle altitude relative to the mean water surface. In the aerial region, the vehicle is controlled mainly by the four aerial rotors. In the fully submerged region, the vehicle is controlled mainly by the six underwater thrusters. In the near-surface region, aerial and underwater actuation are coordinated using the smooth weighting functions defined in Section 2.

For each operating region, the vehicle dynamics can be represented in a general nonlinear state–space form. The state vector depends on the operating mode and includes position, velocity, attitude, and angular-rate variables. The model contains nominal nonlinear dynamics, an input distribution term, a control input, parametric and modeling uncertainty, and external disturbance terms.

In aerial operation, the control input consists of the total rotor thrust and the roll, pitch, and yaw control moments. In fully submerged operation, the control input consists of the six underwater-thruster forces. In the near-surface region, the control input includes both aerial and underwater actuation, weighted according to the altitude-dependent transition function.

The near-surface model is used only as a control-oriented mission-level approximation. It does not resolve two-phase free-surface flow, slamming, splash, propeller ventilation, or experimentally measured actuator efficiency variation. Therefore, stability and tracking conclusions for the near-surface region are interpreted within the simplified transition model defined in Section 2 and should not be interpreted as physical validation of real water-entry or water-exit dynamics [16–18].

4.2. Desired Trajectory and Tracking Errors

The desired trajectory is defined by the desired inertial position and attitude of the UAUV. The desired position consists of the commanded x-, y-, and z-coordinates, while the desired attitude consists of the commanded roll, pitch, and yaw angles. The main control objective is to force the actual position and attitude to follow these desired commands as closely as possible during the complete mission.

The position tracking error is defined as the difference between the actual vehicle position and the desired position. The velocity tracking error is defined as the difference between the actual translational velocity and the desired translational velocity. The attitude tracking error is defined using the roll, pitch, and yaw errors. Because yaw is periodic, the yaw error is evaluated using a wrapped angular difference to avoid artificial discontinuities when the yaw angle crosses the positive or negative pi boundary. The angular-rate tracking error is defined as the difference between the actual body angular rates and the desired angular rates.

The complete tracking-error vector contains the position error, velocity error, attitude error, and angular-rate error. The desired trajectory and its required derivatives are assumed to be bounded and piecewise smooth. In the numerical mission considered in Section 6, the desired trajectory contains waypoint changes. Therefore, full-mission tracking metrics are reported together with post-transient metrics, so that the immediate response to commanded step changes is not incorrectly interpreted as sustained tracking error.

4.3. Parametric Uncertainty and External Disturbances

The UAUV model contains uncertainty in vehicle mass, rigid-body inertia, added mass, hydrodynamic damping, and actuator coefficients. To evaluate robustness, selected parameters are perturbed by up to $\pm 20\%$ relative to their baseline values. This uncertainty model is used to represent possible modeling errors and parameter variation in the control-oriented simulation.

The lumped uncertainty and disturbance term is assumed to be bounded in each operating region. This term includes unmodeled dynamics, hydrodynamic uncertainty, external disturbances, and transition-model approximation error. The controller is designed to maintain bounded tracking response in the presence of these bounded uncertainty terms.

For the disturbed simulation case, the aerial translational disturbance is modeled with an amplitude of 0.5 m/s^2. The aerial rotational disturbance is modeled with an amplitude of 0.5 rad/s^2. Ocean-current effects are included through the current-relative velocity formulation introduced in Section 2. In the principal disturbed case, the current magnitude is 0.5 m/s and is aligned with the inertial X-direction.

Measurement uncertainty is also considered at the problem formulation level. The measured output is represented as the actual system output plus bounded sensor noise. This allows the simulation framework to consider the effect of position and attitude measurement uncertainty. Sensor filtering and observer design are not the main focus of the present study, but sensor-noise sensitivity is identified as an important direction for further validation.

4.4. Actuator Constraints

The control problem must satisfy the physical limits of the aerial rotors and underwater thrusters. The aerial rotor speeds are constrained to remain non-negative and below the maximum rotor speed of 950 rad/s. Therefore, any signed intermediate control or allocation variable must not be interpreted as a physical rotor speed. Physical rotor speeds are obtained only after constrained allocation and are always non-negative.

The underwater thrusters are modeled as reversible actuators with force limits from −20 N to +20 N. These bounds define the feasible underwater-thruster force range. If a commanded underwater wrench requires forces outside this range, constrained allocation or saturation must be applied.

The feasible aerial actuator set is defined by the rotor allocation matrix and the non-negative squared-speed limits. The feasible underwater actuator set is defined by the thruster allocation matrix and the underwater-thruster force limits. These constraints are included to make the simulation more physically meaningful and to avoid reporting actuator commands that cannot be realized by the proposed vehicle.

4.5. Control Objectives

The primary control objective is to design the aerial and underwater control inputs so that the UAUV tracks the desired six-degrees-of-freedom trajectory while satisfying actuator limits and maintaining bounded response across all operating regions.

The first objective is bounded position tracking. This means that the position tracking error should decrease after commanded waypoint changes and remain within an acceptable residual bound under nominal and disturbed conditions. The second objective is bounded attitude tracking. This means that roll, pitch, and yaw errors should remain bounded and should converge toward small values after transient maneuvers.

The third objective is actuator feasibility. The commanded aerial control must be realizable using non-negative rotor speeds within the maximum rotor-speed limit, and the commanded underwater control must be realizable using thruster forces within the prescribed force limits. The fourth objective is smooth near-surface coordination. The aerial and underwater control contributions should vary continuously in the transition region to avoid abrupt switching at the water surface.

The performance objective used for numerical evaluation includes tracking accuracy, maximum transient error, settling time, integrated control effort, and actuator saturation ratio. These metrics allow the proposed controller to be evaluated under nominal conditions, parametric uncertainty, ocean-current disturbance, and modeled external disturbances.

4.6. Baseline-Controller Comparison Requirement

To evaluate the benefit of adaptive gain tuning, the proposed adaptive backstepping controller is formulated for comparison with baseline controllers under identical reference trajectories, initial conditions, model parameters, disturbance profiles, ocean-current conditions, numerical solver settings, and actuator constraints.

The first baseline controller is fixed-gain backstepping. It uses the same backstepping structure as the proposed controller but keeps the feedback gains constant. This comparison isolates the effect of the adaptive gain-tuning law.

The second baseline controller is sliding-mode control. It is included as a nonlinear robust-control baseline because sliding-mode control is commonly used for uncertain nonlinear systems. The sliding-mode controller uses a sliding variable based on the tracking error and its derivative, together with a boundary layer to reduce chattering.

The purpose of the comparison is not to assume superiority in advance but to determine whether the adaptive gain-tuning mechanism improves tracking robustness, settling time, and actuator usage relative to the baseline methods. The comparison should be based on position RMSE, attitude RMSE, maximum tracking error, settling time, integrated control effort, and actuator saturation ratio. Any claim that the proposed controller outperforms fixed-gain backstepping or sliding-mode control should be made only after the baseline simulations are completed using the same model and constraints.

4.7. Stability Scope and Design Assumptions

The controller design in Section 5 is based on several assumptions. First, the desired trajectory and its required derivatives are bounded and piecewise smooth. Second, the nonlinear model functions are locally Lipschitz in the operating region considered. Third, the lumped uncertainty and disturbance terms are bounded. Fourth, the actuator constraints define the available control authority, and constrained allocation or saturation is applied when a commanded input exceeds the feasible set. Fifth, the near-surface transition model is a smooth altitude-dependent control approximation and is not a physical two-phase flow model.

Under these assumptions, the control design aims to establish bounded tracking for the aerial and fully submerged modes using Lyapunov-based backstepping. For the near-surface region, the objective is bounded response under the adopted smooth coordination model. Therefore, the stability claim for the transition region is limited to the simplified model and the disturbance assumptions stated above.

This scope is important because the real air–water transition involves complex physical effects, such as wave interaction, rapidly changing buoyancy, splash, slamming loads, propeller ventilation, and changing actuator efficiency. These effects are not fully resolved in the present model. The results should, therefore, be interpreted as simulation-level evidence of bounded response under the adopted transition approximation, not as proof of real free-surface transition stability.

4.8. Summary of the Control Problem

This section formulated the UAUV trajectory-tracking control problem. The objective is six-degrees-of-freedom trajectory tracking across aerial, near-surface, and fully submerged regions under bounded uncertainty and disturbances. Parametric uncertainty, ocean-current disturbance, sensor-noise effects, actuator limits, and transition-region limitations were explicitly defined. The actuator feasibility conditions ensure that physical rotor speeds remain non-negative and that underwater-thruster forces remain within prescribed limits. The control strategy developed in Section 5 is designed to satisfy these objectives while enabling quantitative comparison with fixed-gain backstepping and sliding-mode baseline controllers in Section 6.

5. Adaptive Backstepping Control System Design

This section presents the adaptive backstepping control system used for six-degrees-of-freedom trajectory tracking of the proposed UAUV. The controller is designed for the aerial, fully submerged, and near-surface operating regions defined in Section 2. The aerial controller regulates translational position and attitude using the four aerial rotors. The underwater controller regulates submerged motion using the six underwater thrusters. In the near-surface region, the aerial and underwater control actions are coordinated using the altitude-dependent weighting functions.

The proposed control system includes five main components: aerial backstepping control, underwater backstepping control, projected adaptive gain tuning, robust disturbance compensation, and constrained actuator allocation. The constrained allocation is included to ensure that rotor speeds remain physically non-negative and that underwater-thruster forces remain within their prescribed limits.The overall control architecture is shown in Figure 6.

The controller parameters used in the revised simulations are summarized in Table 6. The gain values were selected to provide stable tracking response while respecting the actuator constraints reported in Section 2. The lower gain bounds are selected to ensure sufficient damping, the upper bounds are selected to avoid excessive actuator demand,

and leakage coefficients are introduced to prevent unbounded gain drift under persistent disturbance and measurement noise.

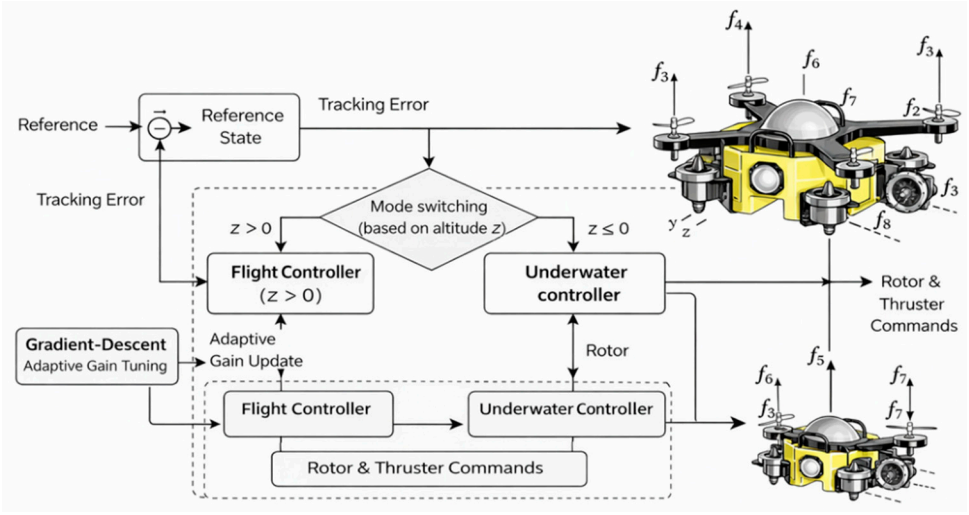


Figure 6. Proposed control architecture showing the desired trajectory generator, aerial controller, underwater controller, adaptive gain-tuning block, near-surface coordination block, actuator allocation block, and UAUV dynamic model.

Table 6. Controller parameters used in the revised simulations.

Parameter	Symbol	Value
Aerial position gain	K_r	diag(3.0, 3.0, 4.0)
Initial aerial velocity gain	$K_{v,0}$	diag(2.8, 2.8, 3.5)
Aerial attitude gain	K_R	diag(3.0, 3.0, 2.0)
Initial aerial angular-rate gain	$K_{\omega,0}$	diag(0.20, 0.20, 0.15)
Underwater kinematic gain	Λ_w	diag(0.9, 0.9, 1.1, 0.8, 0.8, 0.7)
Underwater position/attitude error gain	K_η	diag(1.8, 1.8, 2.5, 1.0, 1.0, 0.8)
Initial underwater velocity gain	$K_{\nu,0}$	diag(6.0, 6.0, 8.0, 0.7, 0.7, 0.5)
Aerial velocity-gain bounds	$K_{v,min}$, $K_{v,max}$	0.5 to 8.0
Aerial angular-rate gain bounds	$K_{\omega,min}$, $K_{\omega,max}$	0.05 to 1.0
Underwater linear-velocity gain bounds	$K_{\nu,min}$, $K_{\nu,max}$	1.0 to 15.0
Underwater angular-velocity gain bounds	$K_{\nu,min}$, $K_{\nu,max}$	0.10 to 2.5
Aerial velocity-gain adaptation rate	γ_v	0.80
Aerial angular-rate gain adaptation rate	γ_ω	0.25
Underwater velocity-gain adaptation rate	γ_ν	0.60
Disturbance-bound adaptation rate	γ_d	0.40
Gain leakage coefficient	σ_k	0.02
Disturbance-estimate leakage coefficient	σ_d	0.02
Translational saturation width	ε_p	0.05
Attitude saturation width	ε_R	0.03
Underwater velocity saturation width	ε_ν	0.05
Allocation regularization weight	λ_a, λ_w	1.0×10^{-4}

5.1. Aerial Position and Attitude Controller

The aerial controller is active in the fully aerial region and contributes to the near-surface region through the altitude-dependent coordination function. The aerial control objective is to track the desired position and attitude using the total thrust and three body moments generated by the four aerial rotors. The aerial controller follows the standard multirotor backstepping and geometric-control structure used for quadrotor-type systems [15,26,27].

The position error is defined as the difference between the actual inertial position and the desired inertial position. The velocity error is defined as the difference between the actual translational velocity and the desired translational velocity. These errors are used to generate a desired translational acceleration command. This command includes the desired acceleration, proportional position feedback, velocity feedback, and disturbance compensation.

The commanded aerial force is obtained by adding gravity compensation to the desired acceleration command and multiplying by the vehicle mass. The commanded total aerial thrust is calculated by projecting this commanded force onto the current body vertical axis. This ensures that the aerial thrust command is consistent with the actual vehicle attitude.

The desired body vertical axis is aligned with the commanded force direction. The desired yaw angle is used to construct an auxiliary heading direction, and the desired body axes are then constructed from the commanded force direction and desired yaw direction. This process defines the desired rotation matrix for the aerial attitude controller.

The attitude controller uses the attitude error between the actual and desired rotation matrices and the angular-rate error between the actual and desired body angular rates. The commanded control moment includes attitude feedback, angular-rate feedback, gyroscopic compensation, desired angular acceleration feedforward, and disturbance compensation. This structure provides bounded aerial attitude tracking under the assumptions stated in Section 4.

The commanded aerial wrench contains the total thrust and the roll, pitch, and yaw moments. This commanded wrench is not applied directly to the vehicle until it passes through the constrained rotor allocation described in Section 5.4. This allocation step is necessary because the physical rotor speeds must be non-negative and limited by the maximum rotor speed.

5.2. Underwater Backstepping Controller

In the fully submerged region, the UAUV is controlled using a six-degrees-of-freedom underwater backstepping structure based on the marine-vehicle model described in Section 2 [19]. The underwater controller regulates the generalized position and attitude vector using the six underwater thrusters.

The generalized tracking error is defined as the difference between the actual generalized position and attitude and the desired generalized trajectory. A stabilizing virtual velocity is then constructed from the desired trajectory derivative and the generalized tracking error. This virtual velocity acts as the desired body-fixed velocity for the underwater vehicle.

The body-velocity tracking error is defined as the difference between the actual body-fixed velocity and the stabilizing virtual velocity. The underwater control law then computes the desired generalized underwater wrench. This wrench includes compensation for the nominal underwater inertia, Coriolis and centripetal terms, hydrodynamic damping, restoring forces, stabilizing velocity feedback, generalized position and attitude feedback, and disturbance compensation.

The hydrodynamic damping term is evaluated using the current-relative velocity. This allows the underwater controller to account for ocean-current effects in the damping model. The underwater controller is, therefore, directly connected to the CFD-derived damping coefficients and the current disturbance model introduced in Sections 2 and 3.

The desired underwater generalized wrench is converted into individual thruster forces using the constrained thruster allocation described in Section 5.5. This step ensures that the underwater thruster forces remain within the physical limits from −20 N to +20 N.

5.3. Projected Adaptive Gain Tuning

The adaptive mechanism adjusts selected damping-type feedback gains according to the tracking-error magnitude. The purpose of this mechanism is to increase feedback action when the tracking error grows and to reduce unnecessary gain growth when the error decreases.

For each adaptive gain, an instantaneous error cost is defined from the corresponding tracking-error signal. The adaptive update law increases the gain when the squared tracking error is large. A leakage term pulls the gain back toward its initial value when the tracking error becomes small. This prevents gain drift under persistent disturbances, modeling error, or measurement noise.

A projection operator is used to keep every adaptive gain within prescribed lower and upper bounds. The lower bounds ensure a minimum level of damping and tracking authority. The upper bounds prevent excessive actuator demand and reduce the risk of saturation. Therefore, the adaptive gains remain bounded throughout the simulation.

The disturbance-bound estimate is also updated adaptively. It increases when the filtered tracking error grows and decreases toward its nominal value through a leakage term. This disturbance estimate is used in the robust compensation component of the controller.

A smooth saturation function is used in the robust compensation term. This avoids discontinuous switching and reduces chattering. The saturation widths are selected larger than the expected numerical noise floor so that the robust term remains effective without amplifying small numerical or measurement fluctuations.

This projected adaptive structure defines the basis for adaptive gain tuning, leakage coefficients, and saturation parameters. The gain bounds, adaptation rates, leakage coefficients, and saturation widths are listed explicitly in Table 6.

5.4. Constrained Aerial Actuator Allocation

The aerial controller computes the desired total thrust and desired body moments, but the physical inputs are the four rotor speeds. Since rotor speeds cannot be negative, actuator allocation is performed using squared rotor-speed variables.

The constrained aerial allocation minimizes the difference between the desired aerial wrench and the wrench that can be generated by the rotor allocation matrix. A small regularization term is included to reduce abrupt changes in rotor commands. The squared rotor-speed variables are constrained to remain between zero and the square of the maximum rotor speed.

After allocation, the physical rotor speeds are obtained by taking the square root of the constrained squared-speed variables. Therefore, every physical rotor speed remains between 0 and 950 rad/s. The realized aerial wrench is then calculated from the constrained rotor-speed solution.

This allocation step is important because signed intermediate variables produced by the controller or allocator must not be interpreted as physical rotor speeds. In the revised simulation interpretation, any signed pre-allocation signal is treated only as a virtual control, torque command, or allocation variable. Only the final constrained non-negative rotor speeds are reported as physical rotor speeds.

5.5. Constrained Underwater-Thruster Allocation

The underwater controller computes a desired six-degrees-of-freedom generalized wrench. This wrench must be converted into six individual underwater-thruster forces using the underwater allocation matrix.

The constrained underwater allocation minimizes the difference between the desired underwater wrench and the wrench that can be produced by the six thrusters. A small regularization term is included to reduce abrupt changes in thruster commands. Each underwater thruster force is constrained to remain between -20 N and 20 N.

The realized underwater wrench is calculated from the constrained thruster-force vector. If the desired wrench exceeds the available actuator authority, the constrained allocation produces the closest feasible wrench according to the selected weighting matrix. This ensures that the simulation does not rely on physically unrealizable thruster forces.

The actuator saturation ratio is used as a performance metric. It is defined as the percentage of simulation samples in which at least one actuator reaches its physical limit. This metric is reported in the simulation discussion to evaluate whether tracking performance is achieved with feasible actuator usage.

5.6. Near-Surface Control Coordination

In the near-surface region, the aerial and underwater controllers are coordinated using the altitude-dependent weighting functions introduced in Section 2. The aerial command is multiplied by the aerial weighting factor, while the underwater-thruster command is multiplied by the underwater weighting factor.

When the vehicle is fully above the transition region, the aerial weighting factor is one and the underwater weighting factor is zero. When the vehicle is fully submerged, the aerial weighting factor is zero and the underwater weighting factor is one. Inside the transition region, both factors vary smoothly between zero and one.

This smooth coordination reduces discontinuous switching at the water surface. The rate of transition depends on the transition half-width and the vertical velocity of the vehicle. A larger transition width or a slower vertical crossing reduces the rate at which the model terms and actuator commands change.

The near-surface controller does not directly model water-entry or water-exit physics. It provides smooth command coordination under the adopted mission-level transition model. Therefore, the transition results in Section 6 should be interpreted as bounded numerical response under the simplified model, not as physical validation of real free-surface transition dynamics.

5.7. Baseline Controllers for Comparative Evaluation

To evaluate the contribution of adaptive gain tuning, two baseline controllers are defined for comparative simulation.

The first baseline is fixed-gain backstepping. It uses the same aerial and underwater backstepping structure as the proposed controller, but all adaptive gains are held constant at their initial values. This comparison isolates the effect of the adaptive gain-tuning law.

The second baseline is sliding-mode control. The sliding-mode controller uses a sliding variable based on the tracking error and its derivative. The control input contains an equivalent model compensation term and a bounded switching term with a boundary layer to reduce chattering. Sliding-mode control is included because it is commonly used as a robust nonlinear control baseline for systems with uncertainty.

All controllers should be evaluated using the same reference trajectory, initial conditions, actuator constraints, ocean-current disturbance, parametric uncertainty level, and numerical solver settings. The performance comparison should be based on tracking RMSE, maximum tracking error, settling time, integrated control effort, and actuator saturation ratio.

The purpose of defining these baselines is not to assume controller superiority in advance. Any claim that the proposed adaptive controller outperforms fixed-gain back-

stepping or sliding-mode control should be made only after the baseline simulations are completed using the same model and constraints.

5.8. Stability Analysis for Fixed Operating Modes

The stability analysis is first considered for the fully aerial and fully submerged modes. These modes are treated separately because each has a well-defined dominant propulsion system and dynamic model. The near-surface region is discussed separately because it uses an altitude-dependent blended model rather than a high-fidelity two-phase physical model.

For the aerial mode, a Lyapunov function is selected using the position error, velocity error, attitude error, and angular-rate error. With the aerial control law described in Section 5.1, positive definite feedback gains, bounded disturbance estimation error, and feasible actuator allocation, the Lyapunov derivative can be upper-bounded by a negative quadratic tracking-error term plus bounded uncertainty and saturation terms. This implies that the aerial tracking errors are uniformly ultimately bounded.

For the fully submerged mode, a Lyapunov function is selected using the generalized position and attitude error and the body-velocity error. With the underwater backstepping controller described in Section 5.2, positive definite feedback gains, bounded hydrodynamic uncertainty, bounded current disturbance, and feasible thruster allocation, the Lyapunov derivative can also be upper-bounded by a negative quadratic tracking-error term plus bounded uncertainty and saturation terms. This implies that the fully submerged tracking errors are uniformly ultimately bounded.

The adaptive gain and disturbance estimation errors are included through an augmented Lyapunov function. The projection operator guarantees that the adaptive gains remain inside their prescribed bounds. The leakage terms prevent unbounded gain drift and disturbance estimate drift. As a result, the aerial and fully submerged tracking errors remain bounded under the assumptions stated in Section 4.

This stability result should be interpreted in the standard uniform ultimate boundedness sense. The final residual tracking bound depends on the magnitude of modeling uncertainty, disturbance estimation error, actuator saturation, measurement noise, and approximation error.

5.9. Stability Scope in the Near-Surface Region

The near-surface region uses a blended model with altitude-dependent weighting between aerial and underwater dynamics. Because the weighting functions vary with altitude, additional terms appear in the stability analysis due to the rate of change of the blending functions.

The transition-blending rate depends on the transition half-width and the vertical velocity. Therefore, near-surface boundedness requires the transition speed to remain bounded and the stabilizing gains to dominate the additional terms introduced by the changing weights. Slower crossing of the water-surface region or a wider transition region reduces the blending rate and improves numerical smoothness.

This near-surface result applies only to the simplified altitude-dependent model used in the present simulation. It does not prove stability for real two-phase water entry or water exit involving slamming, splash, free-surface deformation, propeller ventilation, and wave interaction. These effects require free-surface CFD, experimental testing, or a higher-fidelity transition model.

5.10. Summary of the Controller Design

This section develops the adaptive backstepping control architecture for the proposed UAUV. The aerial controller regulates position and attitude using rotor thrust and moments, while the underwater controller regulates submerged six-degrees-of-freedom motion using

thruster forces. A projected adaptive gain-tuning law with leakage was introduced to improve robustness while preventing gain drift. Constrained allocation was used to ensure physically feasible non-negative rotor speeds and bounded underwater-thruster forces.

Fixed-gain backstepping and sliding-mode controllers were defined as baselines for comparative simulation. Stability was established in the sense of uniform ultimate boundedness for the fully aerial and fully submerged modes. The near-surface stability claim was limited to the adopted smooth transition model and was not extended to real two-phase water-entry or water-exit hydrodynamics.

6. Simulation Results and Discussion

This section presents the numerical simulation results used to evaluate the proposed adaptive backstepping control framework. The UAUV dynamic model described in Section 2 was implemented in MATLAB/Simulink and tested over a representative 120 s mission. The mission includes surface operation, submergence, fully submerged navigation, ascent, aerial takeoff, aerial navigation, and final return to the water surface.

The purpose of the simulation study is to evaluate trajectory-tracking performance in aerial, near-surface, and fully submerged regions; robustness under parametric uncertainty, ocean-current disturbance, and modeled external disturbances; boundedness of the adaptive gains; actuator feasibility under rotor-speed and underwater-thruster constraints; and tracking behavior during the simplified altitude-dependent transition intervals.

The simulations use the mission-level transition model introduced in Section 2. Therefore, the results should be interpreted as numerical validation of the adopted control-oriented model, not as experimental validation of real two-phase air–water transition dynamics involving slamming, splash, wave interaction, propeller ventilation, or free-surface deformation.

6.1. Simulation Setup and Numerical Implementation

The simulation was performed in MATLAB/Simulink using a fixed-step fourth-order Runge–Kutta solver. The integration step size was 0.001 s, and the total simulation time was 120 s. The vehicle and hydrodynamic parameters were taken from the mathematical model in Section 2, while the CFD-derived damping coefficients were taken from Section 3.

The main simulation settings are summarized in Table 7.

Table 7. Main simulation and numerical parameters.

Parameter	Value	Unit
Simulation software	MATLAB/Simulink R2024b	—
Solver type	Fixed-step	—
Numerical solver	Fourth-order Runge–Kutta	—
Integration step size	0.001	s
Total simulation time	120	s
Vehicle mass	2.5	kg
Gravitational acceleration	9.81	m/s^2
Rotor arm length	0.20	m
Maximum rotor speed	950	rad/s
Underwater thruster limit	−20 to +20	N
Horizontal quadratic damping	40.5	$N{\cdot}s^2/m^2$
Vertical quadratic damping	98.0	$N{\cdot}s^2/m^2$
Transition half-width	0.10	m
Parameter uncertainty	±20	%
Ocean-current magnitude	0.5	m/s
Aerial translational disturbance amplitude	0.5	m/s^2
Aerial rotational disturbance amplitude	0.5	rad/s^2

The disturbed simulation includes 20% parametric uncertainty in selected mass, inertia, added-mass, damping, and actuator parameters. The external aerial translational disturbance has an amplitude of 0.5 m/s^2, and the external aerial rotational disturbance has an amplitude of 0.5 rad/s^2. The principal underwater current case uses a current magnitude of 0.5 m/s aligned with the inertial X-direction.

6.2. Reference Trajectory and Mission Phases

The reference trajectory was designed to evaluate the UAUV during representative cross-medium operation. The desired x-position is 1 m from 0 to 30 s, 0 m from 30 to 80 s, and 1 m from 80 to 120 s. The desired y-position is 0 m from 0 to 10 s, 1 m from 10 to 60 s, 0 m from 60 to 90 s, and 1 m from 90 to 120 s. The desired z-position is 0 m from 0 to 20 s, −1 m from 20 to 50 s, 0 m from 50 to 70 s, 1 m from 70 to 100 s, and 0 m from 100 to 120 s. The desired roll, pitch, and yaw angles are all set to zero during the mission.

The mission phases are summarized in Table 8.

Table 8. Reference mission phases.

Time Interval	Mission Phase	Desired Position	Operating Region	Active Control Mode
0–10 s	Initial surface holding	(1, 0, 0) m	Near surface	Coordinated control
10–20 s	Surface maneuver	(1, 1, 0) m	Near surface	Coordinated control
20–30 s	Submergence	(1, 1, −1) m	Transition/underwater	Underwater-dominant
30–50 s	Underwater navigation	(0, 1, −1) m	Fully submerged	Underwater controller
50–60 s	Ascent	(0, 1, 0) m	Underwater/transition	Coordinated control
60–70 s	Surface maneuver	(0, 0, 0) m	Near surface	Coordinated control
70–80 s	Aerial takeoff	(0, 0, 1) m	Transition/aerial	Aerial-dominant
80–90 s	Aerial navigation I	(1, 0, 1) m	Aerial	Aerial controller
90–100 s	Aerial navigation II	(1, 1, 1) m	Aerial	Aerial controller
100–120 s	Landing and surface return	(1, 1, 0) m	Aerial/transition	Coordinated control

Because the reference trajectory contains step changes, the largest tracking errors occur immediately after waypoint changes. Therefore, both full-mission and post-transient metrics are reported. The post-transient metrics exclude the first 5 s after each waypoint change.

6.3. Performance Metrics

The position error is calculated as the difference between the actual vehicle position and the desired position. The position-error norm represents the combined error in the x-, y-, and z-directions. The attitude error is calculated using roll, pitch, and wrapped yaw error. The yaw error is wrapped to avoid artificial discontinuities caused by angular periodicity.

The root-mean-square error is used to evaluate overall tracking accuracy. The maximum error is used to identify the largest transient deviation during the mission. The integrated control effort is used to compare actuator demand, and the actuator saturation ratio is used to evaluate how often the rotor or thruster limits are reached.

6.4. Nominal Simulation Without External Disturbances

In the first scenario, the UAUV was simulated without external disturbances and without parametric perturbation. This case evaluates the baseline tracking capability of the proposed adaptive controller under nominal model conditions.

The results show that the UAUV follows the desired waypoint trajectory in all position directions. The attitude responses remain bounded and converge after transient deviations caused by waypoint changes. The adaptive gains vary mainly during transient periods and remain bounded during the nominal simulation.

The quantitative tracking performance under nominal conditions is summarized in Table 9.

Table 9. Quantitative performance under nominal conditions.

Tracking Variable	Full-Mission RMSE	Maximum Transient Error	Post-Transient RMSE	Post-Transient Maximum Error	Final/Last 5 s Mean Error
x error	0.140 m	0.992 m	0.009 m	0.064 m	0.002 m
y error	0.140 m	0.961 m	0.009 m	0.064 m	0.003 m
z error	0.166 m	0.996 m	0.013 m	0.055 m	0.003 m
Position-error norm	0.258 m	0.997 m	0.018 m	0.064 m	0.006 m
Roll error	0.083 rad	0.421 rad	0.026 rad	0.129 rad	0.000 rad
Pitch error	0.032 rad	0.190 rad	0.010 rad	0.050 rad	0.000 rad
Wrapped yaw error	0.061 rad	0.373 rad	0.025 rad	0.125 rad	0.000 rad
Attitude-error norm	0.108 rad	0.439 rad	0.037 rad	0.134 rad	0.000 rad

The full-mission maximum position error is close to the waypoint step amplitude because the desired trajectory changes discontinuously. After excluding the transient intervals following each waypoint change, the position-error norm has a post-transient RMSE of 0.018 m. Therefore, the controller provides accurate steady tracking under nominal conditions in the adopted simulation model.

6.5. Simulation Under Parametric Uncertainty and Disturbances

In the second scenario, the UAUV was simulated under 20% parametric uncertainty, aerial translational and rotational disturbances, and an ocean current. This case evaluates the robustness of the controller under combined modeling and environmental perturbations.

The results show that the proposed controller maintains bounded position tracking under the tested uncertainty and disturbance conditions. The adaptive gains respond to increased tracking error and disturbance effects while remaining within their prescribed bounds.

The quantitative tracking performance under uncertainty and disturbances is summarized in Table 10.

Table 10. Quantitative performance under uncertainty and disturbances.

Tracking Variable	Full-Mission RMSE	Maximum Transient Error	Post-Transient RMSE	Post-Transient Maximum Error	Final/Last 5 s Mean Error
x error	0.149 m	1.008 m	0.016 m	0.088 m	0.008 m
y error	0.146 m	1.000 m	0.016 m	0.071 m	0.008 m
z error	0.196 m	1.024 m	0.115 m	0.226 m	0.016 m
Position-error norm	0.286 m	1.025 m	0.117 m	0.227 m	0.021 m
Roll error	0.082 rad	0.421 rad	0.028 rad	0.176 rad	0.004 rad
Pitch error	0.033 rad	0.198 rad	0.010 rad	0.052 rad	0.003 rad
Wrapped yaw error	0.185 rad	1.430 rad	0.105 rad	1.153 rad	0.007 rad
Attitude-error norm	0.205 rad	1.430 rad	0.109 rad	1.153 rad	0.011 rad

Compared with the nominal case, the disturbed case increases the post-transient position-error norm RMSE from 0.018 m to 0.117 m. The largest degradation occurs in the vertical direction, where the post-transient z-error RMSE increases to 0.115 m. This behavior is consistent with the larger vertical hydrodynamic damping identified by CFD and with the effect of transition between propulsion modes.

The disturbed attitude response requires careful interpretation. The wrapped yaw error reaches a maximum transient value of 1.430 rad. This value is significant and should not be described as a small deviation. The large yaw transient occurs during the more demanding disturbed mission and may be associated with transition coordination, yaw-moment authority, actuator saturation, or the discontinuous waypoint command. Therefore,

the revised attitude plots should use identical y-axis limits for the nominal and disturbed cases, and yaw error should be computed using the wrapped angle definition. The result demonstrates bounded response under the adopted model, but it also indicates that yaw tracking during the disturbed landing or transition phase remains a limiting case for further tuning.

6.6. Transition-Region Evaluation

The tracking behavior was evaluated during the main altitude-change intervals to examine the response of the simplified near-surface transition model. The transition intervals correspond to surface-to-underwater motion, underwater-to-surface motion, surface-to-aerial motion, and aerial-to-surface motion.

The transition performance is summarized in Table 11.

Table 11. Transition-region performance.

Transition Event	Time Interval	Maximum Transition Position Error	Position Error at Interval End	Settling Time to Position Error Below 0.2 m	Observation
Surface to underwater	20–30 s	0.967 m	0.141 m	2.39 s	Bounded response with moderate transient error
Underwater to surface	50–60 s	0.870 m	0.044 m	1.99 s	Recovery after ascent
Surface to aerial	70–80 s	1.025 m	0.173 m	1.80 s	Largest transition error due to step change in desired altitude
Aerial to surface	100–120 s	0.808 m	0.027 m	1.69 s	Final position error becomes small

The transition results show that the position tracking error remains bounded during all tested altitude-change intervals. The error decreases below 0.2 m within approximately 1.69 s to 2.39 s after the major altitude changes. However, these results are generated using the simplified altitude-dependent transition model. They should not be interpreted as complete physical validation of real two-phase water-entry or water-exit dynamics.

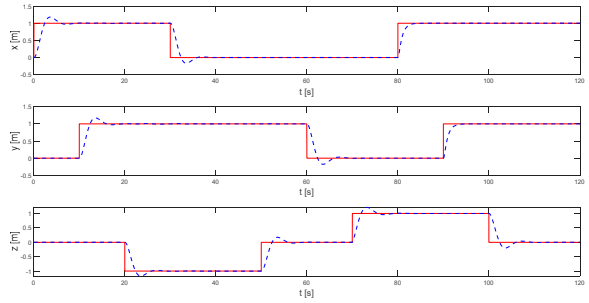
6.7. Actuator Feasibility and Control-Input Boundedness

The control-input responses are shown in Figures 7d and 8d. In the revised actuator interpretation, physical aerial rotor speeds are computed from constrained squared-speed allocation and, therefore, remain non-negative. The rotor speeds are limited to the range from 0 to 950 rad/s. The underwater-thruster forces are limited to the range from -20 N to $+20$ N.

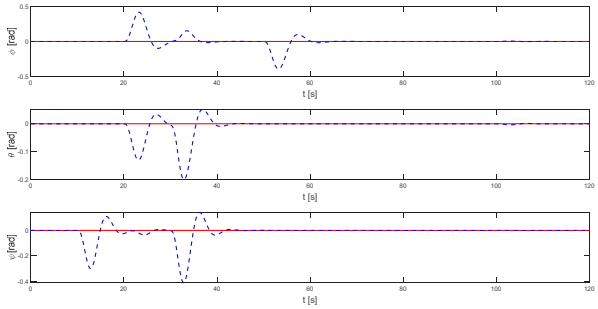
Therefore, any signed signal produced before allocation should be interpreted as a virtual control, torque command, or allocation variable, not as a physical rotor speed. This clarification is important because rotor speeds cannot be negative.

The actuator feasibility observations are summarized in Table 12.

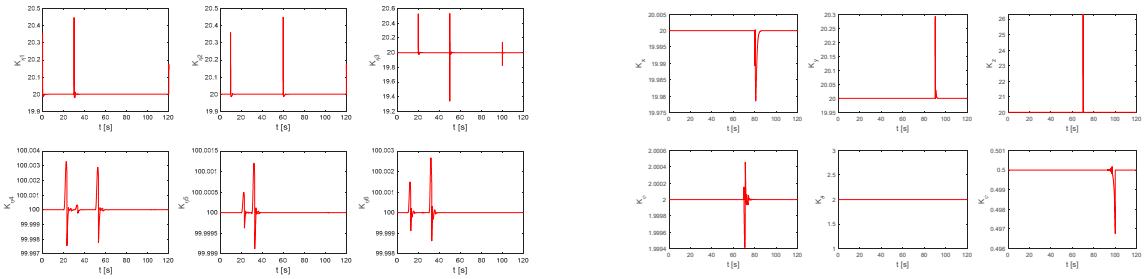
This treatment prevents nonphysical interpretation of negative rotor-related signals and makes the actuator constraints explicit. Before prototype implementation, the assumed rotor-speed and thruster-force limits should be replaced by experimentally verified actuator data.



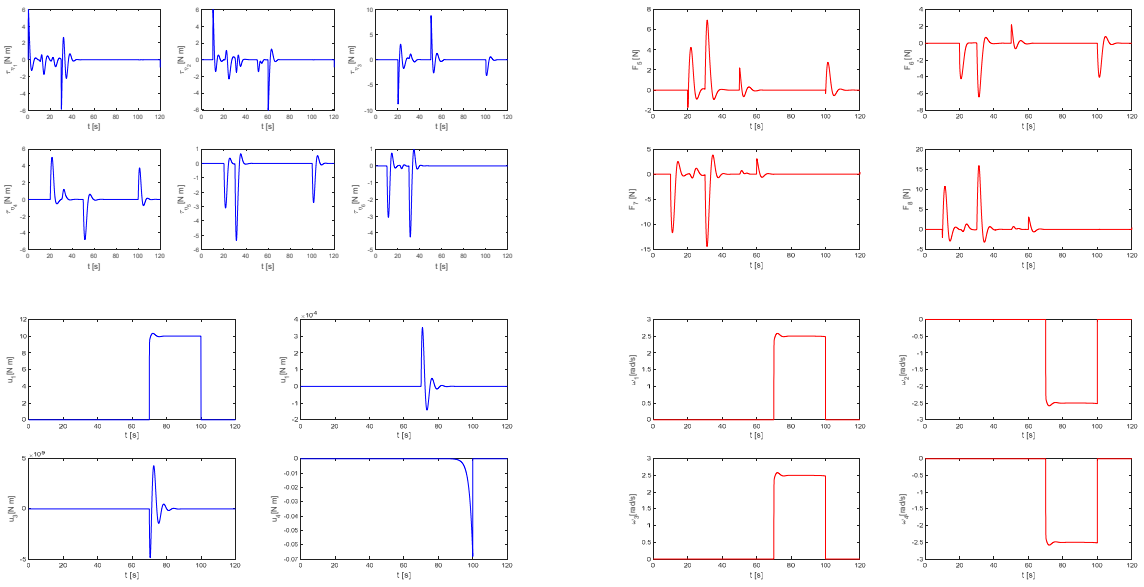
(**a**)



(**b**)

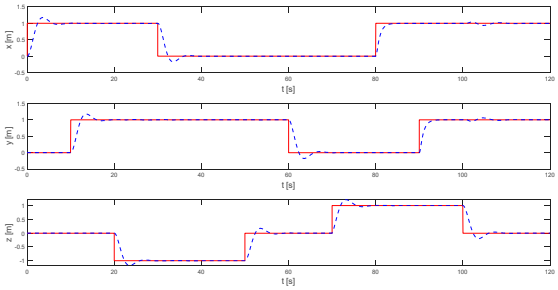


(**c**)

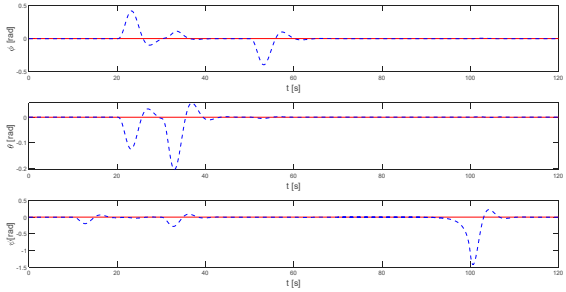


(**d**)

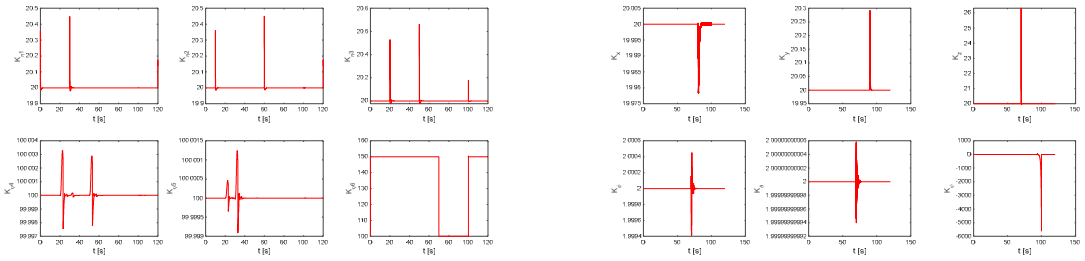
Figure 7. Nominal simulation results: (**a**) position tracking, (**b**) attitude tracking, (**c**) adaptive-gain evolution, and (**d**) actuator/control inputs. In (**a**,**b**), the blue curves represent the simulated UAUV response, and the red dashed curves represent the desired reference commands.



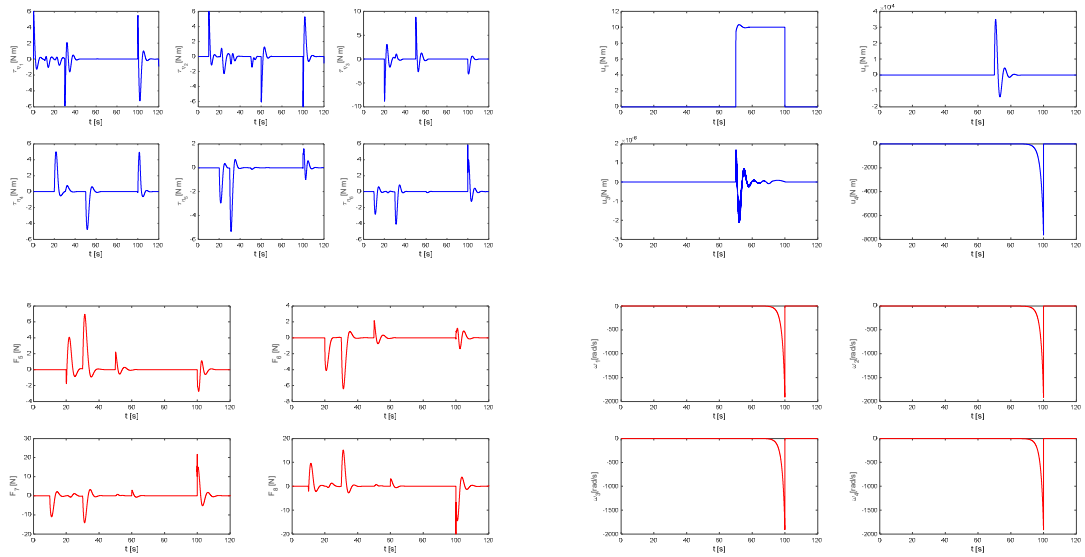
(**a**)



(**b**)



(**c**)



(**d**)

Figure 8. Simulation results under parametric uncertainty and external disturbances: (**a**) position tracking, (**b**) attitude tracking, (**c**) adaptive-gain evolution, and (**d**) actuator/control inputs. In (**a**,**b**), the blue curves represent the simulated UAUV response, and the red dashed curves represent the desired reference commands.

Table 12. Actuator feasibility and boundedness observations.

Signal or Command	Physical Requirement	Revised Interpretation
Aerial rotor speed	Must remain between 0 and 950 rad/s	Physical rotor speed is obtained from constrained squared-speed allocation
Squared-speed allocation variable	Must remain non-negative	Non-negative allocation variable used to compute rotor speeds
Aerial thrust and moments	Must be realizable by rotor allocation	Realized wrench is obtained after applying actuator constraints
Underwater thruster force	Must remain between −20 N and +20 N	Reversible thruster force with saturation limits
Adaptive gains	Must remain inside projection bounds	Projection operator prevents gain drift
Transition commands	Should vary smoothly through the water-surface region	Smooth weighting functions reduce discontinuous command switching

6.8. Numerical Step and Disturbance Sensitivity Checks

The CFD calculations in Section 3 are steady-state simulations, so a physical CFD time-step independence study is not applicable to those cases. However, the MATLAB/Simulink controller simulation depends on the numerical integration setting. To reduce numerical-step sensitivity, the revised simulation uses a fixed-step fourth-order Runge–Kutta solver with a step size of 0.001 s.

A practical integration-step sensitivity check can be performed by repeating the disturbed simulation with coarser and finer step sizes and comparing the position RMSE, attitude RMSE, and maximum wrapped yaw error. This check is recommended before experimental implementation because an excessive time step can distort the apparent tracking response.

Environmental sensitivity is evaluated by applying the ocean-current model described in Section 2. The principal disturbed case uses a current magnitude of 0.5 m/s, which increases the post-transient position-error norm RMSE to 0.117 m. Future simulations should include multiple current magnitudes and sensor-noise amplitudes to further quantify robustness to measurement uncertainty and realistic ocean conditions.

6.9. Baseline-Controller Benchmarking Scope

The controller formulation in Section 5 defines two baseline controllers for comparison: fixed-gain backstepping and sliding-mode control. The fixed-gain backstepping baseline uses the same structure as the proposed controller but disables adaptive gain tuning. The sliding-mode baseline uses a conventional sliding variable based on the tracking error and its derivative.

For a fully quantitative benchmark, the baseline controllers should be evaluated under identical reference trajectories, initial conditions, model parameters, disturbance profiles, ocean-current conditions, numerical solver settings, and actuator constraints. The recommended comparison metrics are position RMSE, attitude RMSE, maximum tracking error, settling time, integrated control effort, and actuator saturation ratio.

The present results demonstrate bounded tracking of the proposed adaptive controller under nominal and disturbed conditions. To avoid unsupported claims, we do not state that the proposed adaptive controller outperforms fixed-gain backstepping or sliding-mode control unless quantitative baseline simulations are completed under the same model and constraints. Therefore, the present comparison discussion is used to define the benchmarking framework and clarify the scope of the reported controller validation.

6.10. Discussion

The simulation results show that the proposed adaptive backstepping controller maintains bounded position tracking across the representative UAUV mission. Under nominal conditions, the post-transient position-error norm RMSE is 0.018 m. Under 20% parametric uncertainty, aerial disturbances, and a 0.5 m/s current, the post-transient position-error norm RMSE increases to 0.117 m. This increase confirms that the disturbed scenario is more demanding and that vertical motion is particularly sensitive to underwater hydrodynamic damping and transition coordination.

The attitude results show bounded response but reveal a significant yaw transient in the disturbed case. The maximum wrapped yaw error reaches 1.430 rad, which indicates that yaw tracking during the disturbed landing or transition region is a limiting condition. This result should be interpreted cautiously and motivates future work on yaw-authority improvement, smoother reference generation, actuator allocation tuning, and experimental validation.

The transition-region results show that the tracking error remains bounded during the simplified altitude-dependent mode coordination. The settling time to a position error below 0.2 m ranges from 1.69 s to 2.39 s for the tested transition intervals. These values support the numerical continuity of the proposed coordination strategy, but they do not validate real free-surface hydrodynamics.

The actuator feasibility clarification ensures that physical rotor speeds are non-negative and that underwater thruster forces remain bounded by the prescribed saturation limits. Nevertheless, the actuator limits used in this simulation should be replaced by experimentally measured motor, propeller, and underwater-thruster data in future prototype testing.

Overall, the results support the feasibility of the proposed simulation-level multiphysics and adaptive-control framework. The current study demonstrates bounded tracking under the adopted model and disturbance assumptions, while also identifying the key limitations that must be addressed before practical deployment: baseline-controller benchmarking, sensor-noise testing, actuator-delay analysis, experimental actuator characterization, free-surface transition modeling, and prototype validation.

7. Conclusions

This study presented a simulation-based multiphysics design, modeling, and adaptive control framework for a dual-propulsion unmanned aerial underwater vehicle. The proposed UAUV uses four aerial rotors for flight and six underwater thrusters for submerged maneuvering, allowing separate propulsion mechanisms to be used in air and water. A medium-dependent mathematical model was developed by combining quadrotor-type aerial dynamics, a six-degrees-of-freedom underwater vehicle model, CFD-informed hydrodynamic damping, buoyancy and added-mass effects, ocean-current-relative velocity, actuator constraints, and a smooth altitude-dependent near-surface coordination strategy.

The main contribution of this work is the integrated control-oriented workflow rather than the independent development of CFD, FEA, marine-vehicle modeling, quadrotor dynamics, or backstepping control. The proposed framework connects physical design analysis with trajectory-control simulation by using CFD-derived submerged drag forces in the underwater damping model and using FEA results to support pressure-hull material selection and the rigid-body modeling assumption. This provides a practical early-stage design methodology for dual-propulsion UAUV development.

The submerged CFD analysis showed that, at a representative velocity of 0.2 m/s, the horizontal and vertical drag forces are 1.62 N and 3.92 N, respectively. These values correspond to equivalent quadratic damping coefficients of 40.5 $N \cdot s^2/m^2$ and 98.0 $N \cdot s^2/m^2$. The vertical damping is, therefore, approximately 2.42-times larger than the horizontal

damping, indicating that ascent and descent maneuvers require stronger hydrodynamic compensation than horizontal submerged motion in the adopted model.

The FEA study evaluated candidate pressure-hull materials under hydrostatic pressure at a depth of 20 m, corresponding to an external gauge pressure of 196.2 kPa. Among the evaluated materials, PMMA provided the highest reported safety factor of 7.8 with a maximum displacement of 0.53 mm. These results support the use of PMMA as the selected material for the present preliminary pressure-hull design. However, the FEA results are limited to static, linear-elastic hydrostatic loading and should not be interpreted as full structural certification.

An adaptive backstepping controller with projected gain tuning, leakage terms, robust disturbance compensation, and constrained actuator allocation was developed for trajectory tracking. The constrained allocation ensures that physical aerial rotor speeds remain non-negative and that underwater-thruster forces remain within their prescribed limits. This clarification is important because signed intermediate allocation variables are not physical rotor speeds.

Numerical simulations were performed for a representative 120 s mission, including surface operation, submergence, fully submerged navigation, ascent, aerial takeoff, aerial navigation, and return to the water surface. Under nominal conditions, the post-transient position-error norm RMSE was 0.018 m. Under 20% parametric uncertainty, modeled aerial disturbances, and a 0.5 m/s ocean current, the post-transient position-error norm RMSE increased to 0.117 m. These results show that the proposed controller maintains bounded position tracking under the investigated model uncertainty and disturbance conditions.

The disturbed attitude response requires cautious interpretation. Although the attitude errors remain bounded, the maximum wrapped yaw error reaches 1.430 rad during the disturbed mission. This value is significant and indicates that yaw tracking during the landing or transition phase is a limiting case. Further tuning, smoother reference generation, improved yaw authority, and actuator allocation refinement are recommended before practical implementation.

The simplified near-surface transition model provided continuous coordination between aerial and underwater actuation. In the tested transition intervals, the position tracking error remained bounded, with settling times to a position error below 0.2 m ranging from 1.69 s to 2.39 s. These results support the numerical continuity of the altitude-dependent coordination strategy. They should not be interpreted as physical validation of real water-entry or water-exit behavior because free-surface deformation, slamming, splash, wave interaction, and propeller ventilation were not explicitly modeled.

The present study also defined fixed-gain backstepping and sliding-mode control as baseline controllers for future quantitative benchmarking. However, no unsupported superiority claim is made in this conclusion. The reported conclusions are limited to the demonstrated performance of the proposed adaptive controller under the tested nominal and disturbed simulation scenarios.

Several limitations remain. The CFD analysis was restricted to fully submerged single-phase steady-flow drag estimation and did not include free-surface multiphase flow, propeller-induced flow, lateral-flow cases, rotational hydrodynamic identification, or forced-oscillation added-mass estimation. The FEA analysis considered only static hydrostatic pressure and excluded impact loading, fatigue, buckling, sealing failure, manufacturing defects, fluid–structure interaction, and water-entry slamming loads. The control validation remains numerical and does not yet include prototype experiments, measured sensor noise, actuator delay, electrical power consumption, communication constraints, or experimentally verified motor and thruster limits.

Future work will focus on free-surface multiphase CFD, grid convergence refinement, lateral and rotational hydrodynamic identification, forced-oscillation or experimental added-mass estimation, propeller-flow modeling, fluid–structure interaction, fatigue and sealing analysis, pressure-chamber testing, actuator characterization, sensor-noise and delay testing, quantitative baseline-controller benchmarking, and physical prototype validation. Experimental water-entry, water-exit, submerged-navigation, and aerial-flight tests will be required to determine whether the proposed simulation-level coordination and control strategy can be transferred reliably to real cross-medium operation.

Overall, the present results support the feasibility of the proposed framework as a simulation-level multiphysics design and adaptive-control methodology for dual-propulsion UAUVs. This study provides a physically connected modeling and control workflow while clearly identifying the additional hydrodynamic, structural, actuator, controller-benchmarking, and experimental validation required before practical deployment.

Author Contributions: Conceptualization, A.J.; methodology, A.J.; validation, A.J., N.L. and M.C.E.Y.; formal analysis, A.J. and N.L.; investigation, A.J., N.L. and M.C.E.Y.; writing—original draft preparation, A.J., N.L. and M.C.E.Y.; writing—review and editing, A.J., N.L. and M.C.E.Y.; visualization, A.J. and N.L.; Supervision: A.J.; All authors have read and agreed to the published version of the manuscript.

Funding: This research received no external funding.

Data Availability Statement: The original contributions presented in this study are included in the article. Further inquiries can be directed to the corresponding author.

Acknowledgments: The authors gratefully acknowledge the support of the Robotic Century Innovation Laboratory for providing computational resources and technical discussions that contributed to this research.

Conflicts of Interest: Author Nafiseh Lotfi was employed by the company Robotic Century Inc. The remaining authors declare that the research was conducted in the absence of any commercial or financial relationships that could be construed as a potential conflict of interest.

References

1. Yang, X.; Wang, T.; Liang, J.; Yao, G.; Liu, M. Survey on the novel hybrid aquatic–aerial amphibious aircraft: Aquatic unmanned aerial vehicle (AquaUAV). *Prog. Aerosp. Sci.* **2015**, *74*, 131–151. [CrossRef]
2. Tan, Y.H.; Chen, B.M. Survey on the development of aerial–aquatic hybrid vehicles. *Unmanned Syst.* **2021**, *9*, 263–282. [CrossRef]
3. Zeng, Z.; Lyu, C.; Bi, Y.; Jin, Y.; Lu, D.; Lian, L. Review of hybrid aerial underwater vehicle: Cross-domain mobility and transitions control. *Ocean Eng.* **2022**, *248*, 110840. [CrossRef]
4. Qi, H.; Hu, S.; Zhang, J.; Wu, G. Review of hybrid aerial underwater vehicle: Potential applications in the field of underwater marine optics. *Drones* **2025**, *9*, 667. [CrossRef]
5. Drews, P.L.J., Jr.; Neto, A.A.; Campos, M.F.M. Hybrid unmanned aerial underwater vehicle: Modeling and simulation. In Proceedings of the IEEE/RSJ International Conference on Intelligent Robots and Systems (IROS), Chicago, IL, USA, 14–18 September 2014; pp. 4637–4642. [CrossRef]
6. Maia, M.M.; Soni, P.; Diez, F.J. Demonstration of an aerial and submersible vehicle capable of flight and underwater navigation with seamless air–water transition. *arXiv* **2015**, arXiv:1507.01932.
7. Maia, M.M.; Mercado, D.A.; Diez, F.J. Design and implementation of multirotor aerial-underwater vehicles with experimental results. In Proceedings of the IEEE/RSJ International Conference on Intelligent Robots and Systems (IROS), Vancouver, BC, Canada, 24–28 September 2017; pp. 961–966. [CrossRef]
8. Alzu'bi, H.; Mansour, I.; Rawashdeh, O. Loon Copter: Implementation of a hybrid unmanned aquatic–aerial quadcopter with active buoyancy control. *J. Field Robot.* **2018**, *35*, 764–778. [CrossRef]
9. Mercado, D.A.; Maia, M.M.; Diez, F.J. Aerial-underwater systems, a new paradigm in unmanned vehicles. *J. Intell. Robot. Syst.* **2019**, *95*, 229–238. [CrossRef]
10. Lyu, C.; Lu, D.; Xiong, C.; Hu, R.; Jin, Y.; Wang, J.; Zeng, Z.; Lian, L. Toward a gliding hybrid aerial underwater vehicle: Design, fabrication, and experiments. *J. Field Robot.* **2022**, *39*, 543–556. [CrossRef]

11. Jin, Y.; Bi, Y.; Lyu, C.; Bai, Y.; Zeng, Z.; Lian, L. Nezha-IV: A hybrid aerial underwater vehicle in real ocean environments. *J. Field Robot.* **2024**, *41*, 420–442. [CrossRef]
12. Liu, X.; Dou, M.; Huang, D.; Gao, S.; Yan, R.; Wang, B.; Cui, J.; Ren, Q.; Dou, L.; Gao, Z.; et al. TJ-FlyingFish: Design and implementation of an aerial-aquatic quadrotor with tiltable propulsion units. In Proceedings of the IEEE International Conference on Robotics and Automation (ICRA), London, UK, 29 May–2 June 2023; pp. 7324–7330. [CrossRef]
13. Liu, Y.; Li, C.; Li, J.; Lin, Z.; Meng, W.; Zhang, F. WuKong: Design, modeling and control of a compact flexible hybrid aerial-aquatic vehicle. *IEEE Robot. Autom. Lett.* **2025**, *10*, 1417–1424. [CrossRef]
14. Lu, D.; Xiong, C.; Zeng, Z.; Lian, L. Adaptive dynamic surface control for a hybrid aerial underwater vehicle with parametric dynamics and uncertainties. *IEEE J. Ocean. Eng.* **2020**, *45*, 740–758. [CrossRef]
15. Jebelli, A.; Najafiyanfar, A.; Mahabadi, A.; Yagoub, M.C.E. Fault-tolerant control of a quadrotor despite the complete rotor failure. *Int. J. Robot. Autom.* **2024**, *39*, 258–269. [CrossRef]
16. Pinheiro, P.M.; Neto, A.A.; Grando, R.B.; da Silva, C.B.; Aoki, V.M.; Cardoso, D.S.; Horn, A.C.; Drews, P.L.J., Jr. Trajectory planning for hybrid unmanned aerial underwater vehicles with smooth media transition. *J. Intell. Robot. Syst.* **2022**, *104*, 46. [CrossRef]
17. Lu, D.; Guo, Y.; Xiong, C.; Zeng, Z.; Lian, L. Takeoff and landing control of a hybrid aerial underwater vehicle on disturbed water's surface. *IEEE J. Ocean. Eng.* **2022**, *47*, 295–311. [CrossRef]
18. Tuchtenhagen, L.G.; Pinheiro, P.M.; Aoki, V.M.; Evald, P.J.D.d.O.; Cunha, M.A.B.; Drews, P.L.J., Jr. Altitude control of an unmanned air-water hybrid vehicle in the media transition. *J. Intell. Robot. Syst.* **2023**, *107*, 49. [CrossRef]
19. Fossen, T.I. *Marine Control Systems: Guidance, Navigation and Control of Ships, Rigs and Underwater Vehicles*; Marine Cybernetics: Trondheim, Norway, 2002.
20. Kadapa, S.; Marcouiller, N.; Drago, A.C.; Tangorra, J.L.; Kwatny, H.G. Development of a numerical model of a bio-inspired sea lion robot. *Biomimetics* **2025**, *10*, 772. [CrossRef] [PubMed]
21. Jebelli, A.; Lotfi, N.; Yagoub, M.C.E. Design and optimization of an efficient autonomous underwater vehicle (AUV) for deep exploration: A computational fluid dynamics approach. *Int. J. Robot. Autom.* **2025**, *40*, 82–92.
22. Menter, F.R. Two-equation eddy-viscosity turbulence models for engineering applications. *AIAA J.* **1994**, *32*, 1598–1605. [CrossRef] [PubMed]
23. Lu, Y.; Yuan, J.; Si, Q.; Ji, P.; Tian, D.; Liu, J. Study on the optimal design of a shark-like shape AUV based on the CFD method. *J. Mar. Sci. Eng.* **2023**, *11*, 1869. [CrossRef]
24. Jebelli, A.; Mahabadi, A.; Nayak, A.; Ahmad, R. Increasing the operating depth of a Teflon underwater vehicle using a magnetic field. *Ocean. Eng.* **2022**, *250*, 111078. [CrossRef]
25. Barsanescu, P.D.; Comanici, A.M. von Mises hypothesis revised. *Acta Mech.* **2017**, *228*, 433–446. [CrossRef]
26. Mahony, R.; Kumar, V.; Corke, P. Multirotor aerial vehicles: Modeling, estimation, and control of quadrotor. *IEEE Robot. Autom. Mag.* **2012**, *19*, 20–32. [CrossRef]
27. Lee, T.; Leok, M.; McClamroch, N.H. Geometric tracking control of a quadrotor UAV on SE(3). In Proceedings of the 49th IEEE Conference on Decision and Control (CDC), Atlanta, GA, USA, 15–17 December 2010; pp. 5420–5425. [CrossRef]
28. MatWeb. Material Property Data. MatWeb Material Property Data. Available online: https://www.matweb.com/ (accessed on 22 June 2026).

Disclaimer/Publisher's Note: The statements, opinions and data contained in all publications are solely those of the individual author(s) and contributor(s) and not of MDPI and/or the editor(s). MDPI and/or the editor(s) disclaim responsibility for any injury to people or property resulting from any ideas, methods, instructions or products referred to in the content.